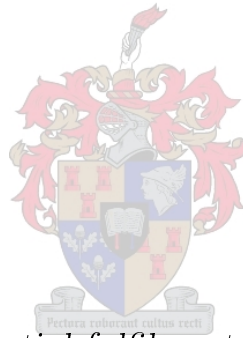# Light Sheet Fluorescence Microscopy

by

Imraan Badrodien

Thesis presented in partial fulfilment of the requirements for the degree of Master of Science (Physics) in the Faculty of Science at Stellenbosch University

Supervisor: Dr. GW. Bosman

Co-supervisor: Dr. PH. Neethling

March 2021

Declaration

By submitting this thesis electronically, I declare that the entirety of the work contained therein is my own, original work, that I am the sole author thereof (save to the extent explicitly otherwise stated), that reproduction and publication thereof by Stellenbosch University will not infringe any third party rights and that I have not previously in its entirety or in part submitted it for obtaining any qualification.

Date: . . . .
March 2021

Abstract

Light Sheet Fluorescence Microscopy

I. Badrodien

*Department of Physical Sciences,
University of Stellenbosch,
South Africa.*

Thesis: MSc (Physics)

March 2021

Light sheet fluorescence microscopy is a powerful tool within the in field of microscopy. The inherent advantages over other fluorescence microscopy techniques include high sectioning capabilities, reduced photo-damage in the sample and short data acquisition times. In this thesis, a light sheet microscope is developed which allows the users to tailor the parameters of the light sheet for various applications, by implementing the use of a spatial light modulator (SLM) to dynamically alter the shape of the light sheet.

Three different techniques for light sheet generation are investigated, namely by the use of a cylindrical lens, using an SLM, and by digitally scanning a beam. Each of the techniques were characterised.

Using the light sheets, three dimensional fluorescence images are obtained. These three dimensional images are analysed to determine the imaging capabilities of the system, and the deconvolution of these images are implemented for image restoration.

The result is a multi-purpose light sheet microscope for use in biological imaging.

Uittreksel

Ligblad Fluoressensie Mikroskopie

("Light Sheet Fluorescence Microscopy")

I. Badrodien

Departement Fisika,
Universiteit van Stellenbosch,
Suid Afrika.

Tesis: MSc (Fisika)

Maart 2021

Ligblad fluoressensiemikroskopie is 'n kragtige tegniek binne die veld van mikroskopiese. Die voordele bo ander fluoressensie-mikroskopie-tegnieke sluit in 'n hoë snyvermoë, verminderde fotoskade in die monster en kort dataverkrygingstye. In hierdie proefskrif word 'n ligbladmikroskoop ontwikkel wat gebruikers in staat stel om die parameters van die ligblad vir verskillende toepassings aan te pas deur die gebruik van 'n ruimtelike ligmodulator (RLM) om die vorm van die ligblad dinamies te verander.

Drie verskillende tegnieke vir ligblad vorming word ondersoek, naamlik deur die gebruik van 'n silindriese lens, met behulp van 'n RLM, en deur 'n ligstraal digitaal te skandeer. Elk van die tegnieke word gekarakteriseer.

Met behulp van die ligblad word driedimensionele fluoressensiebeelde verkry. Hierdie driedimensionele beelde word geanaliseer om die beeldvermoëns van die stelsel te bepaal, en die dekonvolusie van hierdie beelde word geimplementeer vir beeldherstel.

Die resultaat is 'n veeldoelige ligbladmikroskoop vir beeldvorming in biologie.

Acknowledgements

I would like to express my sincere gratitude to my supervisors, Dr Bosman and Dr Neethling, for their guidance and patience during my studies.

I would also like to acknowledge the Council for Scientific and Idustrial Research (CSIR) for funding my studies.

A Special thanks to Phillip Van Heerden for assisting me in matters related to programming and Riyaadh Jamodien for his willingness to assist with any mathematics related questions.

Lastly, I wish to to extend a special thanks to my family and all my friends for their support throughout my studies.

Contents

List of Figures

LIST OF FIGURES viii

List of Tables

Chapter 1

Introduction

1.1   Background

Fluorescence microscopes are popular tools used to image biological samples. These microscopes rely on fluorescence and phosphorescence in order to study small specimens or cell physiology [1]. Fluorescence microscopy allows for the dynamics of cells, tissues and organelles to be visualised [2]. This is achieved by inducing fluorescence within the sample using flourescent dyes to stain the sample, or by attaching flourescent tags to anti-bodies which can target specific features [3].

Fluorophores are molecules which absorb photons of a certain energy and emit photons at lower energies [4]. As illustrated by figure 1.1, this is achieved by exciting the electrons from the ground state into an excited state. The electrons can then undergo vibrational relaxation and internal conversion between states until they decay back to the ground state by emitting a photon. The emitted photon is of a lower energy than the absorbed photon, resulting in a red shift.
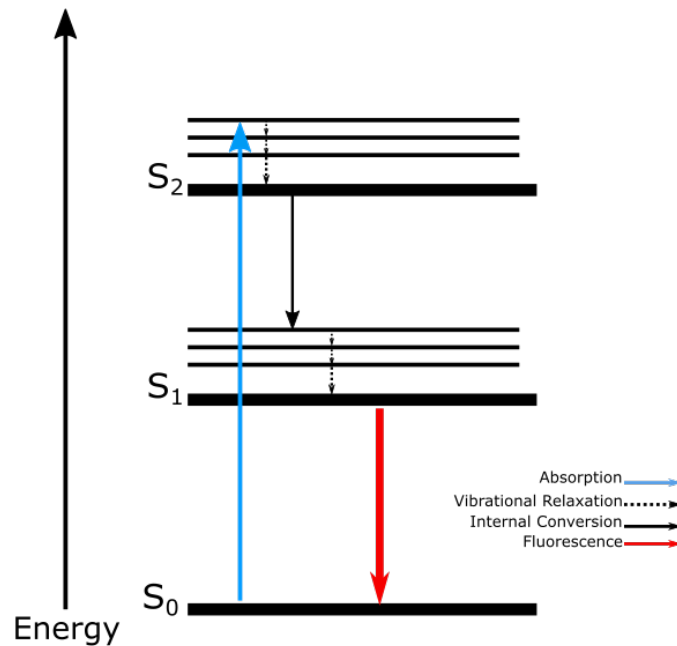
Figure 1.1: Energy level diagram showing the process by which fluorescence is achieved. The excitation to the higher energy levels occurs via absorption of the illumination wavelengths. The excited electron then enters an intermediate state through vibrational relaxation and internal conversion. Finally the ground state is reached by emitting a photon. The emitted photon is usually of a longer wavelength and is seen as fluorescence.

The red shift is essential for fluorescence microscopy as it allows the illumination light to be separated from the fluorescent light by use of appropriate filters [5]. By discriminating between the fluorescent and illumination wavelengths, the resulting image is observed with high contrast against a dark background [5].

The primary concern with imaging biological samples in optical microscopes, after appropriate laser excitation, is induced photo-damage and photo-toxicity. The high intensity of the light, when focused, required to excite fluorescence in the sample could damage or denature biological samples and therefore cause results to be unreliable[6]. For example, using a widefield microscope to image green fluorescent particles (GFP) requires 8 kW/cm^2 of irradiance, while the saturation of the GFP occurs at 11 kW/cm^2 [7].

As illustrated in figure 1.2, traditional point-to-point microscopy scanning techniques, such as those used in confocal microscopes, focus light to a single point within the sample in order to acquire a fluorescence image around the focal point. This results in a large volume of the sample, which is not imaged, to be exposed to the light, causing photo-damage to the cells in these areas [8].
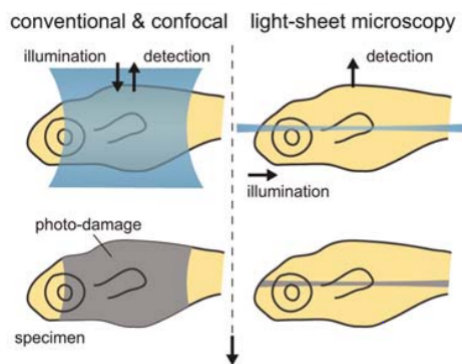
Figure 1.2: Illustration of the photo-damage caused by confocal and conventional microscopy compared with light sheet microscopy. The point-to-point techniques illuminate larger volumes of the sample at a time to acquire images at a single point, whereas light sheet microscopes illuminate only one plane of the sample at a time for imaging. Image taken from Keller and Stelzer [9].

In 1903 the first light sheet microscope was described by Siedentopf and Zsigmondy using sunlight projected through a slit to observe gold particles, however no further development on light sheet microscopes were developed [10]. With the development of the first working laser in 1960, research into and applications of lasers were accelerated [11]. In 1993 the first application of the light sheet micrscope was published by Voie et al [12].

In contrast to confocal microscopes, light sheet microscopes illuminate only a single plane of the sample. The fluorescence from the sample is then collected perpendicular to the plane of the sample which is illuminated by the sheet [13]. Since only one plane of the sample is illuminated and imaged at a time, the photo-damage and photo-toxicity is greatly reduced when compared to point-to-point microscopes [14].

Table 1.1: Comparison of different 3D imaging techniques in vivo imaging of embryos. Data take from Keller and Stelzer [9].

	Light Sheet	Confocal	Two-Photon Excitation
Sectioning Capabilities	In-focus Plane	Entire Specimen	In-focus Plane and Surface
Energy Load	E	10^3E	10^6E
Imaging Speed	63 Mvoxel/sec	2-6 Mvoxel/sec	1 Mvoxel/sec
Signal-to-noise Ratio	1000:1	60:1	10:1

As seen in table 1.1, The sampling of an entire plane also results in faster imaging times [13]. This reduces the illumination time required for imaging, further reducing the induced photo-damage of the sample and therefore allowing longer time periods over which a sample can be imaged [15]. The imaging speed represents the number of voxels which can be imaged within a given time. A single voxel is the smallest three-dimensional space which can be resolved using the system. When compared to confocal microscopes, light sheet microscopes allows for up to 50 times faster imaging speeds and 10-100 times higher signal-to-noise ratio, while illuminating the sample with three orders of magnitude less light [9]. The higher signal to noise ratio seen in light sheet microscopes is due to the illumination of only the imaging plane, and discriminating against the out of focus light.
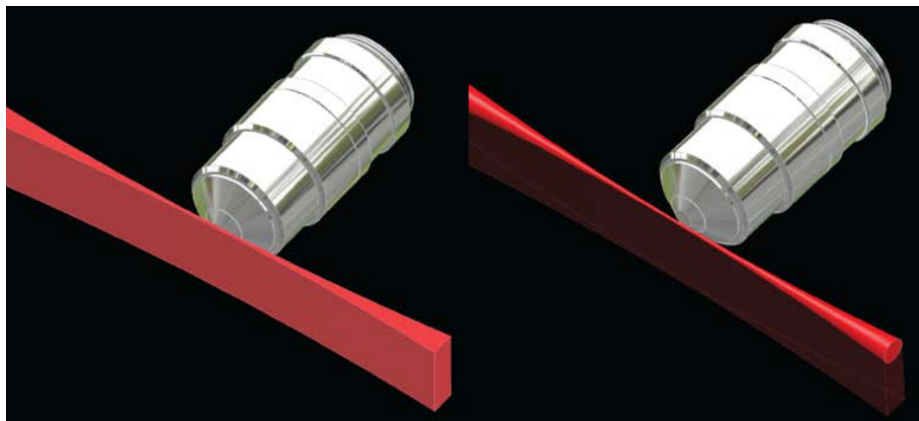
Figure 1.3: Illustration of two methods used to generate light sheets. On the left, a simple light sheet generated using a cylindrical lens and aperture. On the right, a DSLS formed by rapidly scanning a circular beam. Adapted from Gao et al [16].

The methods by which light sheets are generated include the use of cylindrical lenses, such as in the traditional Selective Plane Illumination Microscopes

(SPIM), and digitally scanned light sheets (DSLS). Figure 1.3 illustrates the basic idea of each sheet. Cylindrical lenses are able to focus light along one axis only, resulting in a highly elliptical beam, whereas DSLS are generated by rapidly scanning a circular beam in order to obtain a light sheet [14].

Light sheet microscopes using cylindrical lenses generally only achieve an illumination efficiency of 3% due to severe losses from the apertures, while the absence of such apertures in DSLS results in an efficiency close to 100% [9]. Despite the illumination power of the cylindrical lens systems being constant and uniform, while in DSLS the sheet is illuminated unevenly. The overall effects of photobleaching in traditional light sheet microscopes and DSLS microscopes respectively remain identical [9].

1.2 Aim

The aim of this work is to understand, implement and characterise various techniques of generating light sheets in order to develop a light sheet microscope that can be tailored for a variety of uses. The techniques include the use of commercially available optics and spatial light modulators (SLM) in order to generate static light sheets and digitally scanned light sheets.

1.3 Outline of thesis

An introduction on light sheet microscopy is presented in Chapter 2. The propagation of light along the illumination axis and the parameters affecting the light sheet are introduced in sections 2.2. Sections 2.3 is dedicated to describing the relationships surrounding the imaging systems used in light sheet microscopy. Fourier optics is discussed in sections 2.4, as an introduction to spatial light modulators.

Chapter 3 is dedicated to the techniques and experimental setups used to develop and characterise the various light sheet techniques. The traditional OpenSpim setup is described in sections 3.1, with the use of the SLM for static and scanned light sheets introduced in sections 3.3 and 3.5.

The results of the experiments outlined in chapter 3 are presented and discussed in chapter 4. The sheet parameters obtained using the different techniques are compared. The three dimensional models are reconstructed and analysed in sections 4.8 and 4.9.

A summary and conclusion is presented in chapter 5 along with suggested improvements and proposals for future work.

Chapter 2

Theory

2.1   Fundamentals of Light Sheet Microscopy

While there are many different methods which allow for the generation of light sheets, such scanned beams, the most basic implementation involves the use of a cylindrical lens to generate the light sheet. In this section we will introduce the fundamental principles and parameters of light sheets by using the example of a light sheet generated using a cylindrical lens.

In order to obtain a light sheet, a cylindrical lens can be used to focus a Gaussian beam into a highly elliptical beam. This can be achieved because a cylindrical lens can focus light along one axis only. This highly elliptical beam can then be approximated as planar over a given range. This range is determined by the confocal parameter and is defined as twice the Rayleigh range from the focus of the beam.
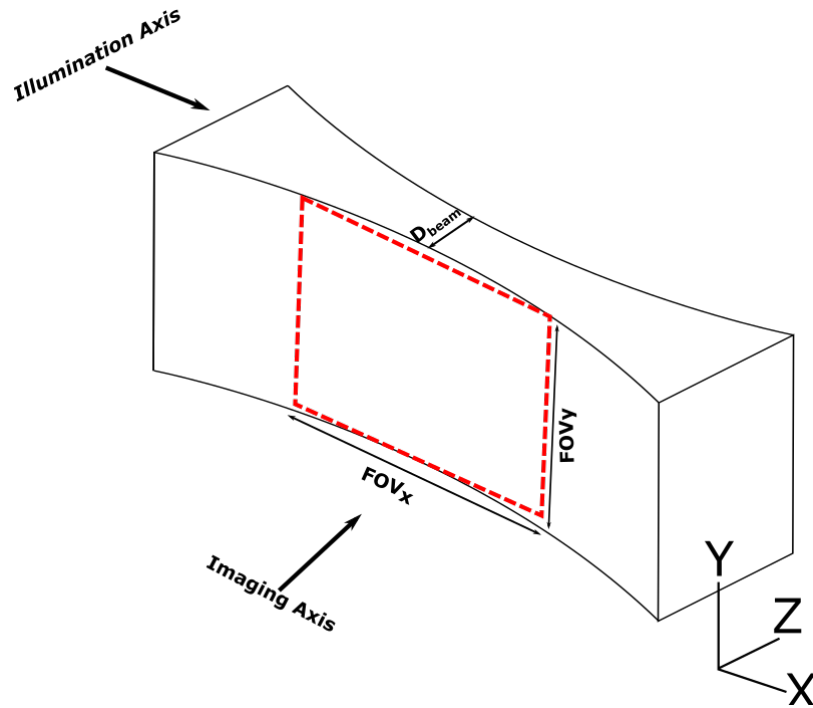
Figure 2.1: Illustration of parameters used to define sheet thickness and field of view, where D_{beam} indicates the sheet thickness, and FOV_x and FOV_y indicate the fields of view in the x and y directions respectively

Using this sheet of light, a suitable sample can then be illuminated. The detection of the fluorescence from the sample is then obtained perpendicular to the plane of illumination as shown in figure 2.1. By moving the sample through the light sheet, multiple images can be collected. These sectioned images are then combined to form a single three dimensional model of the sample.

The parameters of the light sheet microscope can be determined in a number of ways. The thickness and field of view of the light sheet can be defined using Gaussian beam propagation or Fraunhofer diffraction. Since it is experimentally difficult to avoid diffraction and aberration effects from the optics, we will use Fraunhofer diffraction to define our parameters.

2.2 Illumination

In order to explain the illumination and imaging systems, we will discuss the illumination and imaging separately. The methods in the following sections closely follow those described in Light-Sheet Microscopy: a tutorial by Olarte et al [14].

The illumination axis consists of a cylindrical lens which focuses light along one axis. The sectioning capabilities are related to thickness of the light sheet.

It is experimentally not practical to use Gaussian beams, and so apertured beams are used to describe the system. Using the Fraunhofer diffraction pattern for a circular apertures, the field at a distance x from the aperture is given by [17]:

$$E(r) = E_o \frac{2J_1\left(\frac{2\pi ar}{\lambda x}\right)}{\left(\frac{2\pi ar}{\lambda x}\right)} \tag{2.1}$$

where $r = \sqrt{z^2 + y^2}$, a is the radius of the aperture, λ is the wavelength and J_1 is the bessel function of the first kind.

The intensity distribution is therefore

$$I(r) = I_o \left[\frac{2J_1\left(\frac{2\pi ar}{\lambda x}\right)}{\left(\frac{2\pi ar}{\lambda x}\right)}\right]^2 \tag{2.2}$$

The intensity distribution is an airy pattern. The thickness of the sheet will be related to the waist of the beam. The thickness is defined as the extent of the airy beam, that is, the distance between the first two minima of the airy function.

As shown by equation 2.2, the first minimums will occur when

$$\left(\frac{2\pi ar}{\lambda x}\right) = 3.83 \tag{2.3}$$

To define the thickness of the light sheet, we set $y = 0$, such that $r = z$ and $x = f$, where f is the focal length of the objective.

$$\frac{2\pi az}{\lambda f} = 3.83 \tag{2.4}$$

solving for z we then obtain the waist of the sheet as

$$z = \frac{0.61\lambda}{NA} \tag{2.5}$$

The beam diameter, indicated in 2.1, is therefore

$$D_{beam} = 2z = \frac{1.22\lambda_{ill}}{NA_{ill}}, \tag{2.6}$$

where NA_{ill} is the numerical aperture of the illumination lens.

Since the sheet is obtained using a cylindrical lens, the sheet is only focused in the z-axis. The beam remains collimated along the y-axis, and therefore the Field of view along the y-axis (FOV_Y) is determined only by the initial beam diameter before the illumination objective.

For the field of view along the x-axis, the field around the focal plane a distance $x = f$ from the lens with focal length f has the field [18]

$$E(\Delta x) = E_o \frac{sin\left(\frac{\pi\Delta xa^2}{2\lambda f^2}\right)}{\left(\frac{\pi\Delta xa^2}{2\lambda f^2}\right)}, \tag{2.7}$$

where Δx is the distance from the focal position along x. Equation 2.7 has the form of a *sinc* function. The intensity profile is therefore given by the $sinc^2$ function:

$$I(\Delta x) = I_o sinc^2\left(\frac{\pi\Delta xa^2}{2\lambda f^2}\right) \tag{2.8}$$

The zeroes of the $sinc^2$ function occur when $\left(\frac{\pi\Delta xa^2}{2\lambda f^2}\right) = \pi$.

Using $NA \approx \frac{nD}{2f} = \frac{na}{f}$ to solve for Δx, produces the radius from the centre of the $sinc^2$ function to the first zero as:

$$\Delta x = \frac{2\lambda n^2}{NA^2}, \tag{2.9}$$

where NA is the numerical aperture. The distance between the zeroes of the function is then given as [14]

$$2\Delta x = \frac{4\lambda n^2}{NA^2}. \tag{2.10}$$

The field of view along the x-axis will be given by the full width at half maximum (FWHM) of the central lobe of this $sinc^2$ function in order to be consistent with a focused Gaussian beam's confocal parameter. The confocal parameter of a Gaussian beam is equal to the FWHM of the axial intensity distribution of a Gaussian beam.

The field of view is therefore given by [14]:

$$FOV_x = \frac{1.78n\lambda_{ill}}{NA_{ill}^2}, \tag{2.11}$$

where λ_{ill} and NA_{ill}^2 is the illumination wavelength and numerical aperture of the illumination objective respectively.

Equations 2.6 and 2.11 show that the parameters of the light sheet can be adjusted by changing the numerical apperture of the illumination system. A trade off between field of view and sheet thickness is evident due to the numerical apperture dependence. By increasing the numerical apperture, a narrower beam can be achieved, however this results in a shorter field of view.

2.3 Imaging

The imaging axis acts perpendicularly to the illumination axis as shown in figure 2.1. The light emitted from or reflected off of the sample can be magnified by passing the light through a series of lenses and imaged onto a detector. In this section we will discuss the principles of imaging the fluorescence from the sample.

Using a "4f" configuration, we can use simple ray tracing as shown in figure 2.2 to describe the system.
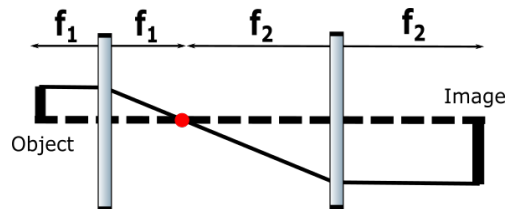
Figure 2.2: A simple 4f configuration for imaging. The first lens (with focal length f_1) is placed a distance f_1 from the object. A second lens (with focal length f_2) is placed at a distance $f_2 + f_1$ from the first lens. The resulting image is then formed a distance f_2 after the second lens, with the image magnified by a factor of $M = \frac{f_1}{f_2}$.

Using the configuration shown in figure 2.2, the image of the object is magnified by a factor of M. With simple ray tracing it can be shown that the magnification factor in a "4f" configuration is given by the ratio of the two focal lengths.

This assumes an idealised system with thin lenses. In reality the illumination axis consists of an objective lens and a tube lens, with a filter to separate the illumination and fluorescent light. As such, experimental results will vary from this model, however we will continue to use this model to approximate the system.

The magnification of the illumination axis is therefore given by [14].

$$M = \frac{f_{\text{TL}}}{f_{\text{obj}}}. \tag{2.12}$$

Where f_{TL} and f_{obj} are the focal lengths of the tube lens and objective respectively.

The resolution of a microscope is defined as the shortest distance between two points on a sample that can be distinguished. When a point source is observed through an aperture, the image takes the form of an airy pattern as a result of Fraunhofer diffraction [17]. The resolution is determined by the Rayleigh Criterion, which states that the shortest distance between two points that can be resolved is given by

$$\sigma = \frac{0.61\lambda}{\text{NA}} \approx 0.61\lambda \tag{2.13}$$

where σ is the shortest distance between the two points, λ is the wavelength, NA is the numerical aperture and R_T is the transversal resolution.

The transversal resolution for detection (R_{Tdet},resolution in xy-plane) is given by the Rayleigh Criterion, equation 2.13:

$$R_{Tdet} = \frac{0.61\lambda}{NA} \approx 0.61\lambda. \tag{2.14}$$

where λ is the wavelength emitted from the sample, and NA is the numerical aperture of the detection objective [14].

Here R_{Tdet} is the maximum transverse resolution allowed by the detection objective, assuming infinitesimal pixels.

The axial resolution (R_{Adet}, along the z-axis) is calculated in a similar way as the FOV of the illumination axis (equation 2.7-2.11) and is given by [14]:

$$R_{Adet} = \frac{1.78n\lambda_{em}}{NA_{em}^2}, \tag{2.15}$$

where λ_{em} is the emission wavelength. The FOV of the camera is given by [14]:

$$\text{FOV}_{\text{camera}} = \text{pix.spix}, \tag{2.16}$$

where pix and spix are the number of pixels and the size of each pixel on the detector.

The imaged pixel size will therefore be

$$\text{spix}_\text{imaged} = \frac{\text{spix}}{M}.$$ (2.17)

Applying the Nyquist sampling Criterion [14], the maximum resolution is therefore

$$R_T = 2\text{spix}_\text{imaged}.$$ (2.18)

Ideally we would like the axial resolution of the imaging system to match the sheet thickness and the FOV of the imaging system (FOV_camera) to match that of the light sheet (FOV_x), however this is difficult to achieve experimentally. In addition these expressions for the detector assume the spacing between pixels to be zero.

2.4 Fourier Imaging

A key property of lenses is the ability to produce a Fourier transform of the light from the back focal plane in the focal plane of the lens. This concept can be used to allow further degrees of freedom when generating light sheets. In this section we will introduce the basic concepts of Fourier imaging and go into further detail in the following sections on how we can take advantage of these concepts when generating light sheets.

To describe the Fourier properties of lens, we will follow the steps described in Introduction to Fourier Optics by J.W Goodman [19]. The description will be done in two dimensions (x and z), where x can be seen as the distance from the propagation axis-z, which can easy be extended to three dimensions.
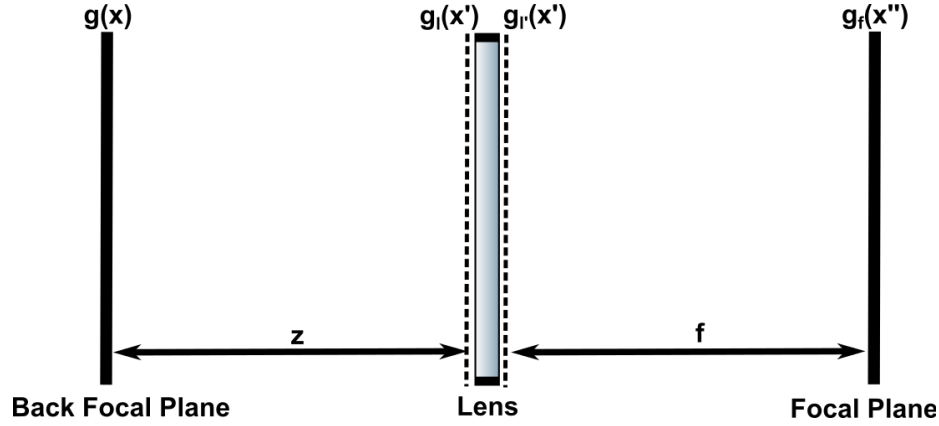
Figure 2.3: Illustration used to describe the field behaviour in a single lens system. The initial field $g(x)$ at the back focal plane of the lens can be described using Fourier properties of propagation in order to determine the field incident on the lens $g_l(x')$. The field emerging from the lens, $g_{l'}(x')$ is given by the transfer function of the lens acting on the incident field. The field at the focal plane of the lens $g_f(x'')$, is then described using Fresnel diffraction and is found to be related to the initial beam via a Fourier transform.

Suppose we define a field $g(x)$ as shown in the figure 2.3. Using the Fourier properties of propagation we have that the Fourier transform of the field $g_l(x')$ incident on the lens is

$$G_l(\rho) = H(\rho)G(\rho), \tag{2.19}$$

where $G(\rho)$ is the Fourier transform of the initial field $g(x)$ and

$$H(\rho) = e^{ikz}e^{-\frac{ikz\lambda^2}{2}\rho^2} \tag{2.20}$$

is the transfer function over the region before the lens with the spacial frequency $\rho = \frac{x}{z\lambda}$ and wavenumber $k = \frac{2\pi}{\lambda}$. A transfer function is a mathematical function that models a material that acts on an input to produce a corresponding output.

The transmission function of a thin lens is given by

$$t(x) = e^{ik\Delta_o}e^{ik(n-1)\Delta(x)} \tag{2.21}$$

where $\Delta(x)$ is the thickness function of a thin lens given by

$$\Delta(x) = \Delta_o - \frac{x^2}{2}\left(\frac{1}{R_1} - \frac{1}{R_2}\right). \tag{2.22}$$

Δ_o is the thickness of the lens at its center, and R_1 and R_2 are the radius of curvature of the two surfaces of the lens.

Using the lens makers formula,

$$\frac{1}{f} = (n-1)\left(\frac{1}{R_1} - \frac{1}{R_2}\right) \tag{2.23}$$

we can then obtain the lens transmission function

$$t_l(x') = e^{-\frac{i\pi x'^2}{f\lambda}}. \tag{2.24}$$

Where the constant phase term has been omitted. The field emerging from the lens $g_l'(x')$ is then given by the transmission function of the lens acting on the incident field $g_l(x')$.

$$g_l'(x') = g_l(x')t_l(x') \tag{2.25}$$

The field is affected by Fresnel diffraction, and the resulting field at a distance f from the lens is given by

$$g_f(x'') = \frac{1}{if\lambda}e^{ikf}\int_{-\infty}^{\infty} g_l'(x')e^{\frac{i\pi(x''-x')^2}{f\lambda}}\,dx' \tag{2.26}$$

Substituting equation 2.25 we have

$$g_f(x'') = \frac{1}{if\lambda}e^{ikf}e^{\frac{i\pi x''^2}{f\lambda}}\int_{-\infty}^{\infty} g_l(x')e^{\frac{-2i\pi x''x'}{f\lambda}}\,dx' \tag{2.27}$$

where we note that the integral is the Fourier transform of $g_l(x')$. From the paraxial approximation we have that $x'' \approx x$ for $k = \frac{2\pi}{\lambda}$. Using this along with equation 2.19 and 2.20, we find that

$$g_f(x'') = \frac{1}{if\lambda}e^{ik(f+z)}e^{\frac{i\pi x''^2}{f\lambda}(1-\frac{f}{z})}G(\rho) \tag{2.28}$$

Setting $z = f$ we have

$$g_f(x'') = \frac{1}{if\lambda}e^{2ikf}G(\rho) \tag{2.29}$$

Therefore we find that a lens produces a Fourier transform of the incident field in the focal plane. This allows us to manipulate optical fields at the focal planes of lenses by filtering the input field. [19]

Another important property of Fourier transforms is the convolution theorem. Suppose we have two function u and v, a convolution is an operation on the two functions that yields an output function of u modified by v. Mathematically this is given as

$$\mathcal{F}(u * v) = \mathcal{F}(u)\mathcal{F}(v) \tag{2.30}$$

and

$$\mathcal{F}(uv) = \mathcal{F}(u) * \mathcal{F}(v) \tag{2.31}$$

where $\mathcal{F}$ represents the Fourier transform and $*$ is the convolution operator. The Image of an object can be seen as the convolution of the objects function and an instruments response, also called the point spread function (PSF). The PSF describes the propagation of light emitted by a point source through the optics to an array detector [20].

Solving the inverse problem allows the reconstruction of the emitting source. This process is known as deconvolution. This process will be described in further details in section 2.7.

Understanding these basic principles of Fourier optics allows us to incorporate the use of spatial light modulators for the generation of light sheets. The following chapter goes into further detail on the methods of spatially modulating these fields.

2.5 Spatial Light Modulators

A static light sheet generated using fixed optics limits the freedom to tailor the sheet sufficiently without changing lenses and objectives. An alternative approach involves the use of a spatial light modulator (SLM) in order to shape the beam profile to generate the sheet of light.

An SLM is a device used to modulate amplitude, phase or polarisations of light waves [21]. The SLM systems are based on translucent or reflective liquid crystal micro-displays.

By applying an external electric or magnetic field to these liquid crystals the orientation of these can be controlled. [21]. This in turn causes a change in the refractive index of the molecules. By defining a certain grayscale to represent voltages across the liquid crystal cell, an image can be formed on the SLM to modulate the light. This image is referred to as a mask.

These masks are usually grayscale images with values ranging from 0 to 255, representing 0 to 2π phase shifts.

When a mask is displayed on the SLM, the light reflected off the SLM is modulated and the Fourier transform of the mask is generated in the focus of

a lens after the SLM as shown in the previous section. In our system we will only use phase modulation.

In the following subsections we will introduce a few basic phase masks and discuss their applications within light sheet microscopy.

2.5.1 Grating Masks

The SLM has a finite size and number of pixels. The light reflected from the SLM surface causes an unwanted diffraction pattern. The center of this diffraction pattern is on the optical axis, and therefore needs to be removed. In order to ensure we have predominantly modulated light, we can collect the light from the first order, resulting in greater power loss. Alternatively, a grating mask can be used to displace the modulated light in the zeroth order from the unwanted reflected light. This greatly improves the efficiency of the system.

The phase mask, producing a grating in the x-direction, is described by

$$\phi(x) = tan\theta x \tag{2.32}$$

where $tan\theta$ is the grating coefficient. This effectively dictates the frequency of the grating. This mask is then wrapped from $-\pi$ to π in order to generate the mask.

The mask can be rotated to adjust the direction of the first order, and this is easily achieved by defining the phases $\phi(x)$ and $\phi(y)$. The resulting mask is then simply given as the sum of these two phases.

In figure 2.4, the effects of a grating mask is shown. A Gaussian amplitude mask is placed on the grating to emulate the region of the SLM illuminated by the incoming beam.
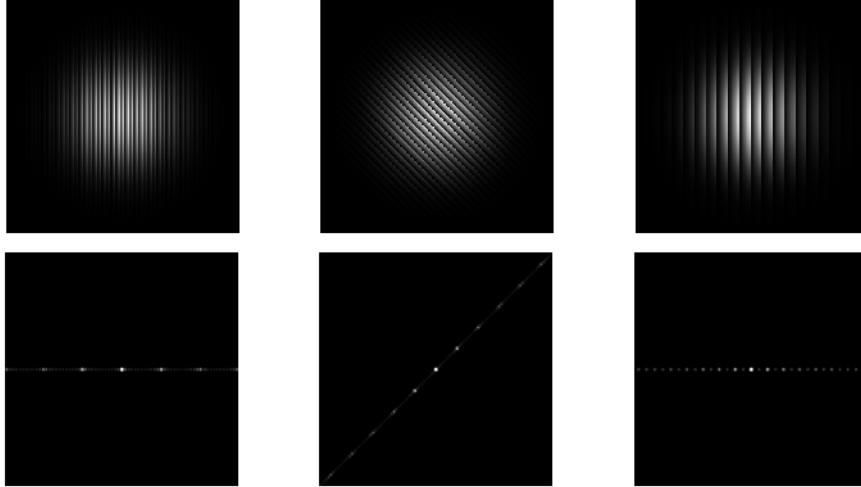
Figure 2.4: The Grating mask on the left has $\theta = 10°$. In the center, the mask has $\theta = 10°$ and is rotated by 45°. The grating on the right has $\theta = 45°$

As seen in figure 2.4, by controlling the grating coefficient we are able adjust distances from the zeroth order to where the modulated beam forms. We are also able to adjust the angle with which these shifts occur.

This allows us to shift our modulated beam to any position. In doing so we are able to separate the modulated light from the unmodulated light in the zeroth order.

2.5.2 Cylindrical Lens Masks

The simplest implementation of a light sheet involves the use of a cylindrical lens to produce a highly elliptical beam. By using an SLM in place of a cylindrical lens, we can emulate the behaviour of the cylindrical lens, while having the freedom to alter the focal lengths without changing optics.

The transmission function for a cylindrical lens is given by

$$T(x) = e^{ikx^2/2f} \tag{2.33}$$

In order to generate an appropriate mask, we define our transmission function by

$$T(x) = e^{ik4\lambda x^2/(Np)^2} \tag{2.34}$$

Where k, N and p is the wavenumber, width of the central zone (in pixels) and the pixel size respectively. Here our transmission function is defined by the number of pixels in the central zone as shown in figure 2.5
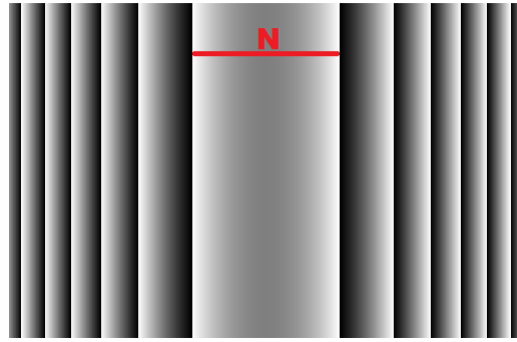
Figure 2.5: Example of a cylindrical lens mask. Here N is the central width of the mask

The masks are again simulated using a Gaussian amplitude mask to indicate the illuminated regions of the mask as shown in figure 2.6.
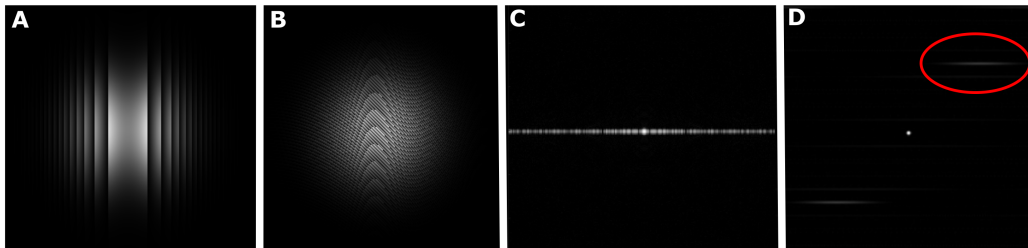
Figure 2.6: The implementation of the cylindrical lens mask. A shows a cylindrical lens mask with a Gaussian amplitude mask, with the resulting Fourier transform in C. A grating is applied to the mask in B, with the resulting Fourier transform shown in D. The parts of the beam used for the light sheet can then be selected using an aperture as shown in D.

Image A shows the cylindrical lens mask, with N = 50, and its corresponding Fourier transform is shown in C. From image C it is difficult to distinguish the shape of the beam as the vertical cylindrical mask produces horizontal elliptical beams which interfere with each other. To avoid this, we add a 45° grating to the phase mask as shown in image B. The resulting Fourier transform then produces the image shown in D. Using an aperture, the desired light can be selected for use as the light sheet as indicated by the red circle.
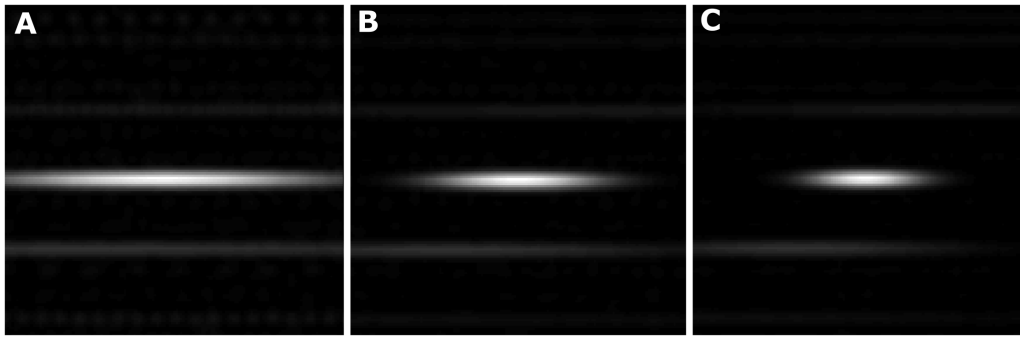
Figure 2.7: Examples of the resulting Fourier transforms of cylindrical lens masks for varying central widths N. Here A,B and C have N = 50, 100 and 150. All the masks have gratings applied to the mask to shift them away from the zeroth order, and the image is cropped around the desired beam as shown in figure 2.6

As seen in figure 2.7, by adjusting the central width of the mask (N) the severity of the ellipse can be controlled. For larger N values the beam profile becomes less elliptical. While not obvious in the images, the central width of the mask will influence the sheet thickness. This can be seen by comparing equations 2.33 and 2.34. By adjusting the central width N, the focal length of the emulated lens is controlled, and therefore the thickness of the sheet can be manipulated.

2.5.3 Axicon Masks

One drawback when generating light sheets is the trade-off between the sheet thickness and the field of view as shown in chapter 2.2. An alternative solution is to incorporate the use of non-diffracting beams in order to maintain small sheet thicknesses while obtaining larger fields of view.

A bessel beam is non-diffractive, allowing these beams to overcome the limitation of the Rayleigh range seen in Gaussian beams [9].
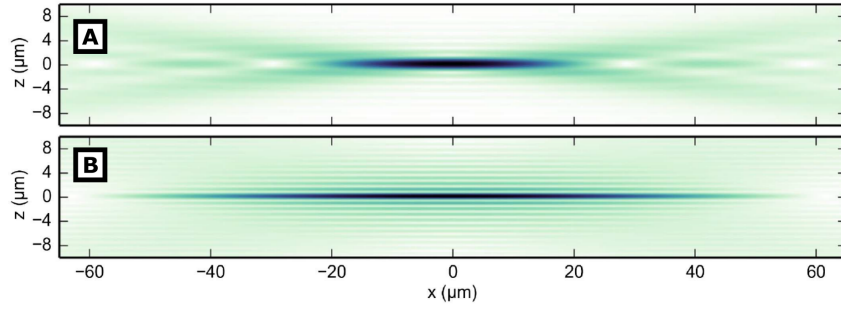
Figure 2.8: Illustration showing the sheet thickness and field of view for Gaussian (A) and Bessel (B) beams. The sheets thicknesses are similar, but the field of view available with the bessel beam is roughly doubled that of the Gaussian beam. Image taken from Olarte et al [14]

.

As shown in figure 2.8, a bessel beam is able to achieve similar sheet thicknesses, while obtaining larger fields of view.

While a true bessel beam cannot be generated, approximations to a bessel beam can be achieved in different ways. The most common methods are the use of an annular aperture, diffraction gratings with cylindrical symmetry [5], or by focusing a Gaussian beam through an axicon lens.

By using the SLM, we can generate an axicon phase mask to approximate a bessel beam.

The transmission function of a single axicon groove is [22]:

$$t(r) = exp(-ik(n-1)r\frac{h}{d})$$ (2.35)

where r is the radial position, k is the wave number, n is the refractive index and $\frac{h}{d}$ is the base angle.

The phase mask is then generated as a convolution between this transmission function and a Dirac-comb function [22] as shown in the figure below.
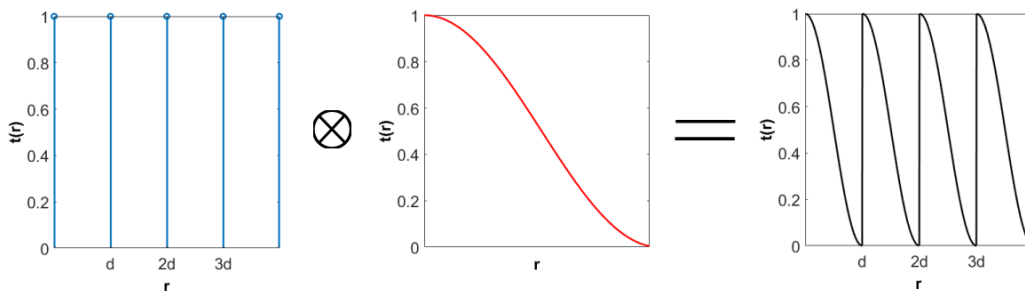
Figure 2.9: Illustration of the convolution between the Dirac-comb function and the transmission function used to generate the axicon in matlab.

The mask has circular symmetry, and so the final mask can be generated by defining the width of the central groove d. Example of masks and the simulated bessel functions are shown in figure 2.10
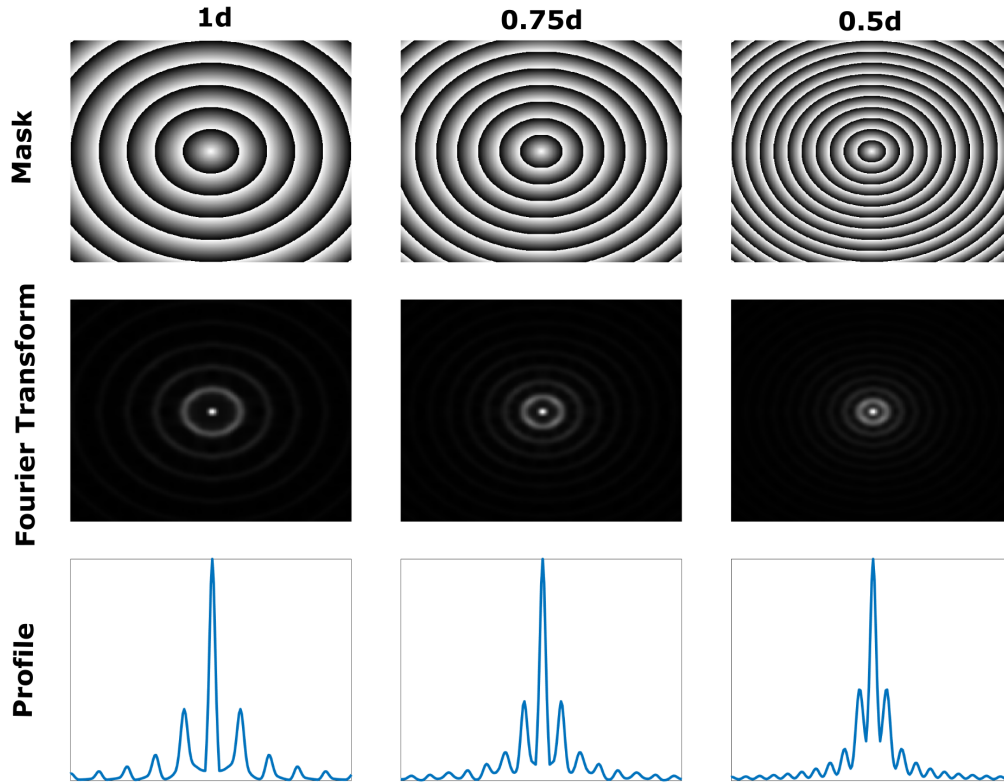
Figure 2.10: Example of masks generated with varying central widths

As shown in figure 2.10, adjusting the central width d, for a constant h, changes the base angle of the axicon. The increase of the central width d is equivalent to a decrease in the base angle of an axicon [22]. The intervals between the rings of the bessel beam increase with an increase in d and thus the frequency of the rings decrease.

This allows us to simulate different axicons using the same optical system which will be convenient for our applications.

The incorporation of the bessel beam will be done using the DSLM approach.

2.6   Dynamic Light Sheets

As illustrated in figure 1.3, it is possible to generate light sheets by rapidly scanning a beam along one axis.

This is typically achieved using galvonometer mirrors, which are rotated by applying a voltage. By sending an oscillating signal to the galvonometer mirrors, the beam can be translated rapidly as shown in figure 2.11

Figure 2.11: Illustration of the operation of a galvonometer. The angle with which the beam is offset is determined by the amplitude of the signal.
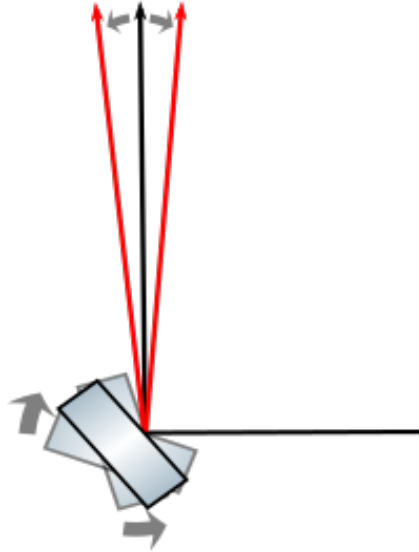
The amplitude of the oscillations determines the angle by which the beam is offset. This angle is chosen such that the beam is translated near parallel to the optical axis at the sample.

The frequency of the oscillations are then set such that the camera, along the detection axis, has an exposure time equal to an integer multiple of a single scan period [14].

$$t_{ex} = N \frac{1}{f_{galvo}} \tag{2.36}$$

Where f_{galvo}, N and t_{ex} are the frequency of the galvonometers, an integer multiple of a single period, and the exposure time of the camera respectively.

This ensures that all the sites of the sample are illuminated equally during a single measurement.

The benefit of dynamic light sheets is that the full intensity is available at each position of the sample as the beam is scanned, where as static light sheets have the intensity distributed over the entire region covered by the sheet.

2.7 Deconvolution

As introduced in section 2.4, distortions in images can be represented mathematically as a convolution of the objects function and the response of the system. In this section we will introduce the reverse function, known as deconvolution.

Deconvolution is an image restoration process. This mathematical process attempts to reassign diffracted light to its source [23]. Deconvolution is therefore related to the setup required to form the image.

The PSF is the image of a single point source of light. The PSF describes the response of the optics in the imaging system [23]. The ability to correctly describe the PSF greatly affects the extent to which the image can be improved.

In the article "Deconvolution of light sheet microscopy recordings" by Becker et al, software for deconvolution in light sheet microscopy is developed [24]. The following section will briefly discuss the methods by which the LsDeconv software deconvolves light sheet microscopy images and how we can apply this software in the system.

While it is possible to measure the PSF of a system, a more convenient approach is to model the PSF. This is because the measurement of the PSF itself is limited by the resolution of the system and the detector array [24]. The light scattered by the imaging medium further limits the ability to adequately measure the PSF [24].

By using a theoretical PSF based on the optics of the image formation in light sheet microscopy, the process of measuring the PSF can be avoided. The LsDeconv software develops a PSF based on the parameters of the system.

The PSF for the Detection system is given by [24]:

$$H_{det}(x,y,z) = 4 \left| \int_0^1 J_o \left(\frac{2\pi}{\lambda_{em}} \frac{NA_{obj}}{n} \sqrt{x^2+y^2} \rho_o \right) e^{i\frac{\pi\rho^2 z NA_{obj}^2}{\lambda_{em} n^2}} \rho_o d\rho_o \right|^2 \quad (2.37)$$

where H_{det} is the detection PSF defined by the zero order Bessel function (J_o), the numerical aperture of the objective(NA_{obj}), the refractive index (n) and the emitted wavelength (λ_{em}). and $\rho_o = \sqrt{x_o^2+y_o^2}$ with $\rho = \sqrt{x^2+y^2}$.

The PSF of the light sheet is given by

$$H_{il}(x,y=0,z) = 4 \left| \int_0^1 J_o \left(\frac{2\pi}{\lambda_{ill}} \frac{NA_{LS}}{n} z\rho_o \right) e^{i\frac{\pi\rho^2 x NA_{LS}^2}{\lambda_{ill} n^2}} \rho_o d\rho_o \right|^2 \quad (2.38)$$

Where H_{il} is the PSF for the light sheet, NA_{LS} is the numerical apperture of the light sheet and λ_{ill} is the illumination wavelength.

The full PSF of the microscope is then given by the element-wise product of equations 2.37 and 2.38 as

$$H_{LSM}(x, y, z) = H_{det}(x, y, z) \cdot H_{il}(x, y = 0, z) \tag{2.39}$$

Figure 2.12 shows the ability of the software to generate point spread functions as acquired in the article by Becker. The agreement seen between the intensity profiles of the measured and calculated PSF's show that the software is able to generate suitable point spread functions for use in light sheet microscopy.
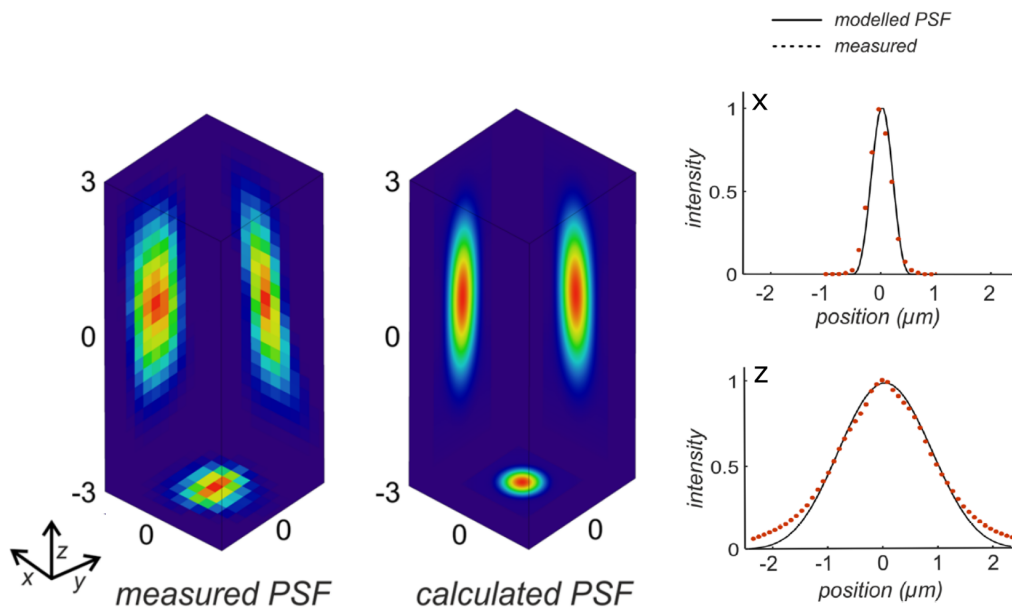
Figure 2.12: The measured and calculated PSF using the LsDeconv software. The intensity profiles along x and z are shown with y=0 for both the measured and generated PSF. Taken from [24]

Using the generated PSF, the deconvolution is done by the Richardson-Lucy algorithm [24]. The Richardson-Lucy algorithm assumes the image is a convolution between the desired image, the generated PSF and Poisson noise. The assumption of Poisson noise is due to the quantum nature of light, in that the detection of photons , by photodetection devices, is a Poisson process with a variance equal to the mean counted photons [25].

The algorithm attempts to generate an improved image that best matches the recorded data when the improved image is convolved with the PSF. This is

repeated iteratively, with each iteration generating correction factors which are used to obtain the estimate for the following iteration.
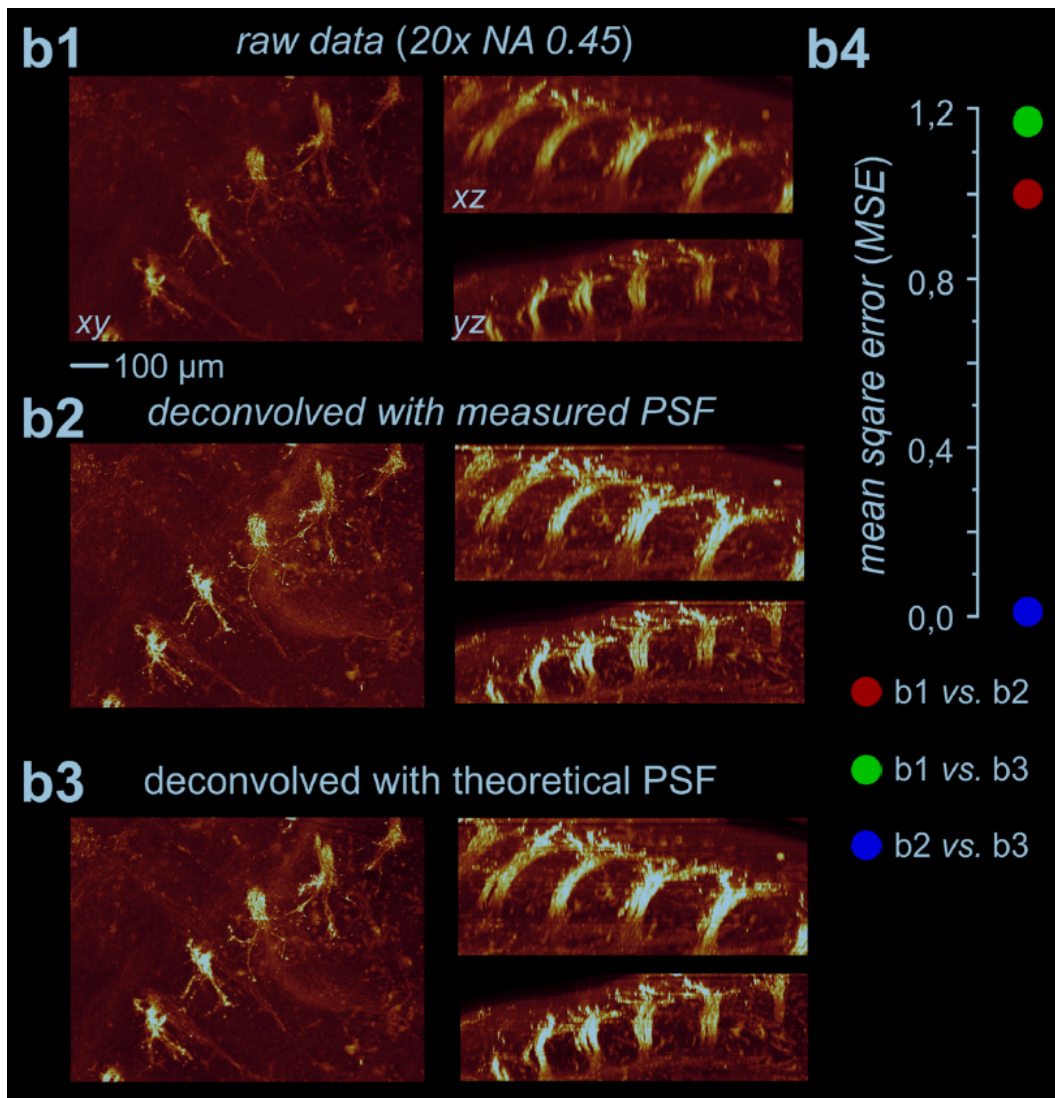
Figure 2.13: Results obtained by Becker et al [24] showing the capabilities of the LsDeconv software. A mean squared error is calculated between the raw data and each of the point spread functions. Taken from Becker et al [24]

The results of the deconvolution algorithm obtained by Becker is shown in figure 2.13. Visually b2 and b3 look identical. The mean squared deviations (MSD) between the raw and deconvolved images were calculated. The deviations between the raw data (b1) and the deconvolution result with the measured PSF were found to be 85.5%, while the deviation between the raw data and the deconvolved data using the theoretical point spread function was 100%. The MSD between the two deconvolved images are found to be 0.95%.

The 0.95% deviation between the two deconvolved data sets indicate that the results of the deconvolution using the measured and theoretical PSF were similar.

The LsDeconv software is therefore a useful tool which can be used to deconvolve the raw images acquired using a theoretical PSF.

Chapter 3

Experimental Setup

In this chapter, the experimental setups used are described. A variety of setups were implemented in order to illustrate the different parameters discussed in chapter 2. The setups to generate light sheets using a cylindrical lens, SLM and scanned beams are discussed in the first 3 sections. This is followed by the setups required to image and measure the light sheet parameters.

3.1 The Cylindrical Lens Light Sheet Microscope Setup

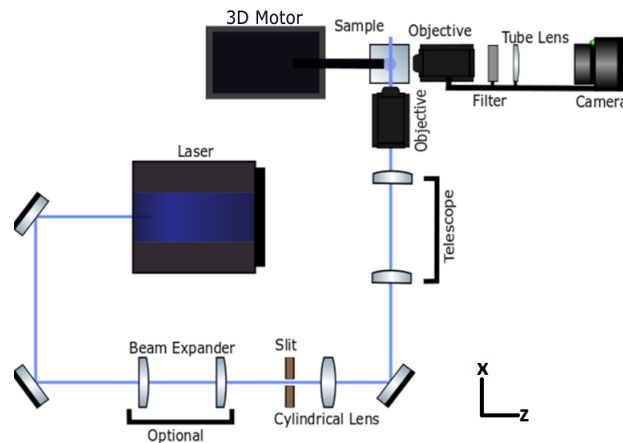The setup for the light sheet microscope is show in figure 3.1.

Figure 3.1: The layout of the cylindrical lens light sheet microscope.

The setup utilises a collimated laser beam which is sent through an adjustable rectangular aperture. The laser is a diode laser with a wavelength of 405 nm

and a power of 25 mW as it enters the system. The low power entering the system is a result of the beam cleaning process to correct for the elliptical output beam of the diode laser. The rectangular aperture positioned at the focal length distance before the cylindrical lens. The cylindrical lens is positioned at its focal length away from a 45° mirror and is rotated such that the cylindrical lens will focus the beam in the y-axis at the surface of the mirror. The beam then passes through a telescope which decreases the scale of the beam before passing through the objective.

The beam emerging from the objective will be focused into a vertical sheet of light where the sample will be mounted. The sample is mounted onto a three-dimensional stage which will allow for the sample to be positioned and moved through the light sheet in order to acquire the cross-sectional images of the sample.

The detection axis, is positioned perpendicular to the plane of the light sheet. The fluorescence from the sample will be collected and imaged by the detection objective and tube lens onto the camera. A filter (bandpass filer,405 ± 8 nm) is placed along the detection axis which will allow only the fluorescent wavelengths to pass through the filter while blocking the illumination light.

We would like to construct a microscope capable of imaging samples around 10 to 30 μm in size. For this purpose we will use a lens instead of an objective.

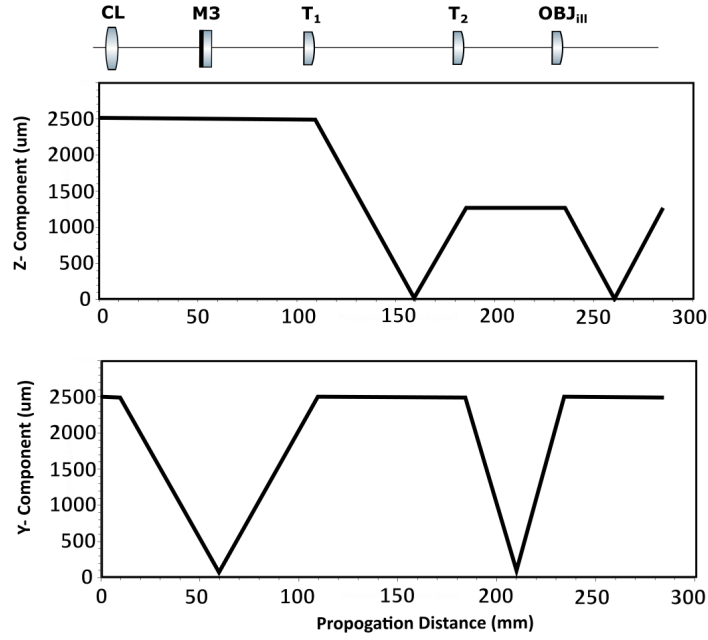As shown in figure 3.1 the x-axis is the propogation axis of the beam.

Figure 3.2: Illustration of the expected behavior of the beam along the illumination axis, obtained using the vWaistwatcher software. Where CL represents the cylindrical lens, M3 represents the mirror after the cylindrical lens, T1 and T2 are the first and second telescope lenses, and Obj$_{ill}$ is the illumination objective. The top chart shows the behavior of the z-component of the beam, while the bottom chart shows the behavior of the y-component of the beam.

Figure 3.2 shows the behaviour of the beam through the system. Due to the presence of the cylindrical lens, the beam appears asymmetric at the focal plane of the objective

The cylindrical lens (CL) is orientated such that the beam is focused in the y-axis. Since the focal length of the cylindrical lens is 50 mm we can determine the numerical aperture of the cylindrical lens as

$$NA_{cyl} = \frac{nD}{2f} = 0.05, \tag{3.1}$$

using $n = 1$.

The thickness of the sheet light sheet at the focus of the cylindrical lens is therefore determined from equation 2.6

$$D_y = \frac{1.22\lambda}{NA_{cyl}} = 9.88 \ \mu m. \tag{3.2}$$

The y-component of the beam on the mirror (M3) will therefore be $9.88 \mu m$, while the z-component will remain at 5mm, since it passes through the cylindrical lens without being focused as shown in figure 3.2.

A 50 mm lens (T1) and a 25 mm lens (T2) will be used in the telescope, placed in a "4f" configuration. This combination will results in the telescope having a magnification of $M = 0.5$. Since the first lens in the telescope is positioned at its focal length away form the mirror, the y-component of the beam emerging from the telescope will be focused at a distance of 25 mm after the second lens in the telescope. The emerging z-component will still be collimated after the telescope, however with a diameter of 2.5 mm.

The final lens (Obj$_{ill}$ in the illumination branch is then positioned 2.5 mm after this focal point. The resulting beam will have a collimated y-component with a beam size of 5 mm, while the z-component of the beam will be focused. The diameter to which the z-component is focused is calculated as

$$NA_{ill} = \frac{nD}{2f} = \frac{2.5}{50} = 0.05, \tag{3.3}$$

$$D_{beam} = \frac{1.22\lambda}{NA_{cyl}} = 9.88 \ \mu m. \tag{3.4}$$

The combination of telescope lenses and the illumination lens chosen for this assembly would result in the numerical aperture, along the z-component, of the illumination lens being identical to that of the cylindrical lens. This should result in a theoretical sheet thickness equal to that calculated from the cylindrical lens. The resulting beam will be seen as a vertical sheet of light.

The FOV of the light sheet is calculated by equation 2.11. The resulting light sheet has a FOV in the x-direction of

$$FOV_x = \frac{1.78 * 405nm}{0.05^2} = 288.36 \ \mu m. \tag{3.5}$$

This provides a theoretical limit for the minimum sheet thickness and field of view of a light sheet which can be generated using this combination of objectives.

Incorporating the variable rectangular aperture allows for the z-component of the incident beam to be adjusted independently of the y-component. We can assume that the diameter of the beam incident on the cylindrical lens is approximately the same size as that of the aperture. By adjusting the slit width, the amount of light incident on the cylindrical lens can be controlled. This allows us to directly control the numerical aperture of the cylindrical lens to manipulate the sheet thickness and FOV.

This setup should adequately allow us to study the parameters affecting the light sheet, however using different wavelengths of light causes chromatic abberations with a single lens which may be accounted for by use of good objectives.

3.2 Setup For Generating Static Light Sheets Using SLM

The setup used to generate static light sheets is shown below.

The SLM used in the setup is a Holoeye Pluto 3.1. The phase masks are generated using Holoeye Pattern Generation Software and the open source SSPIM Matlab Toolbox [26].

Table 3.1: Holoeye Pluto Specifications

Display Type	Reflective LCSO (Phase Only)
Resolution	1920×1080
Pixel Pitch	8.0 μm
Fill Factor	0.93
Active Area	15.36×8.64 mm
Frame Rate	60 Hz

The setup functions similarly to the previous static light sheet setup using a cylindrical lens. A 50/50 beam splitter is used to separate the light going to and from the SLM. A lens with a focal length of 100 mm is placed such that the Fourier transform of the mask displayed on the SLM is formed in the focal plane. An aperture is inserted at the focal plane, where the desired portions of the beam can be selected and imaged at the focal plane of the illumination objective.
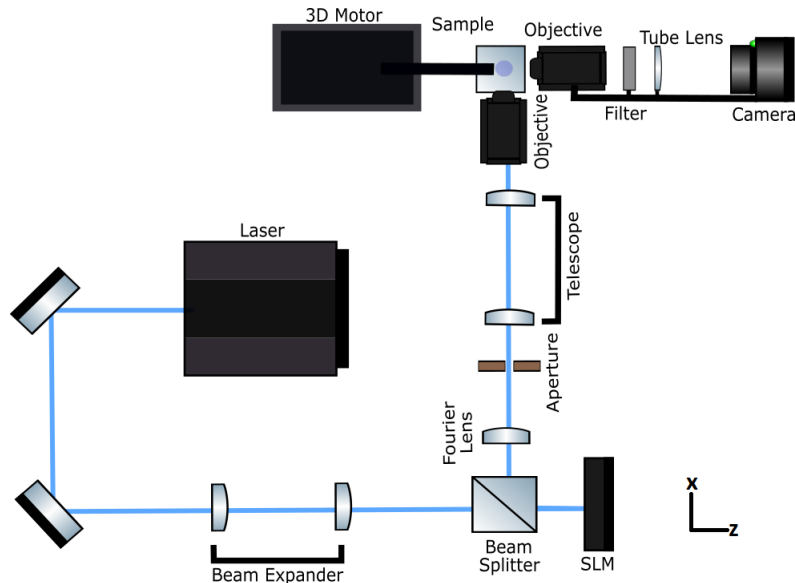

Figure 3.3: Setup used to generate light sheets using an SLM

3.2.1 SLM Calibration

Before generating masks for the SLM it is important to ensure that the SLM to correctly calibrated. This is done to ensure that to full grey scale range, 0 to 255, correctly shifts the phase by 2π.

The self-referenced method is used to check the calibration of the SLM [27]. The SLM's surface area is divided into two zones. One side of the mask is set to as a reference, while the other half has a grey scale value which can be varied. The divided mask will form an interference pattern in the focal plane of the Fourier lens. By imaging this pattern we can visually observe the phase shift as we ramp up the grey level of the one half of the mask. Once a full 2π shift has occurred we can note the grey scale value of the shift and scale the grey levels accordingly to represent a 2π shift.
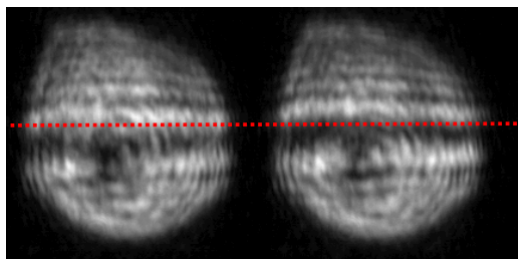

Figure 3.4: Example of the observed phase shifts using self-referenced calibration

Figure 3.4 shows an example of the observed phase shifts. The red line in the image indicates the initial position of the horizontal line. We can see that by ramping up one side of the mask, a phase shift is induced as demonstrated by the shift in the horizontal line in the image.

Holoeyes pattern generation software incorporates its own calibration based on the wavelength of the beam.

When analysing the phase shift, a 2π phase shift occurs at gray scale value 248. The scale factor is therefore given by

$$S = 255/g = 255/248 = 1.03 \tag{3.6}$$

where g is the grayscale value after a 2π shift.

This can be used as a global grayscale factor and implemented to rescale the behaviour on the SLM. In our implementation, it is however not necessary to implement this calibration. The scale factor of 1.03 would have no noticeable impact on our ability to shape the beam, as spacial beam shaping on wavelengths different to the calibration wavelength of the SLM is possible, at the cost of a reduced efficiency [28].

3.3 Experimental Setup for scanned light sheets

The setup used to generate scanned light sheets are shown in figure 5.4 below. The setup closely follows the experimental setup as in the previous section, however galvonometer mirrors are used for scanning the beam.

The galvo system used is a Thorlabs Large Beam Diameter Dual-Axis Scanning Galvo Systems. By applying a voltage signal to the galvonometer system orientation of the mirrors can be controlled.
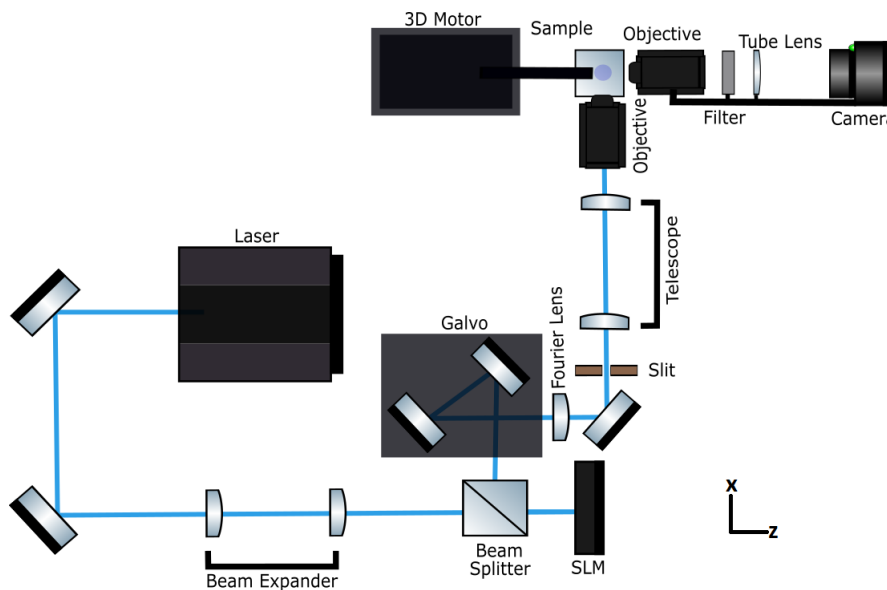
Figure 3.5: Setup used to generate light sheets using a galvonometer for beam scanning

Table 3.2: Thorlabs Dual-Axis Scanning Galvonometer System

Beam Diameter	10 mm
Max Mechanical Scan Angle	20 °
Small Angle Step Response	400 μs
Analog Position Signal Input Range	±10 V
Mechanical Position Signal Input Scale Factor	1.0 V, 0.8 V or 0.5 V per degree

A triangle wave signal is used to scan the beam. This ensures the beam is scanned at a constant speed through a single oscillation. When selecting the scan frequencies and amplitude for the system, care should be taken to ensure the scan frequency is chosen such that the exposure time on the detection

camera is an integer multiple of a single scan period of the beam as described in section 2.6.

3.4 Characterisation of the lightsheet

Characterisation of the light sheet is done in a number of ways. In this section we will briefly outline the methods by which the characterisation of the light sheets are done.

3.4.1 Imaging Setup

The light sheet thickness is measured using the setup shown in figure 3.6.
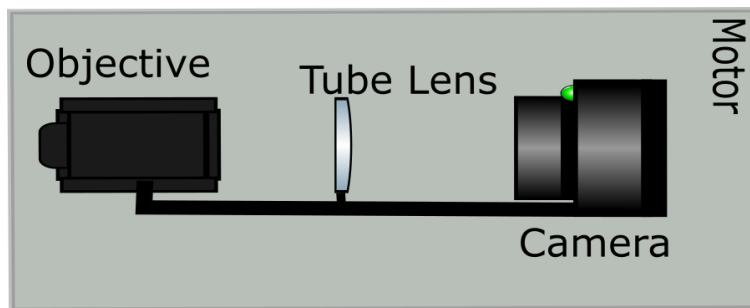

Figure 3.6: Image of the setup used to characterise the sheet thickness and field of view.

The imaging setup utilitises a 10x microscope objective, a 125 mm tube lens and a Thorlabs CMOS camera.

The Specifications of the CMOS camera are shown below

Table 3.3: Thorlabs CMOS detector specifications

Pixel Array	1280×1024
Pixel Size	$5.2 \times 5.2 \ \mu m^2$
Effective Area	$6.656 \times 5.325 \ mm^2$
Full Res Max Frame Rate (fps)	40

This setup is mounted using rails to a one dimensional motor and aligned along the x-axis near the focal plane of the sheet. By scanning through the sheet (along the x-axis), images of the sheet (in the yz-plane) are acquired.

From these images, the sheet thickness can be measured over a distance along the x-axis. The field of view is then calculated using this data, and defined as twice the Rayleigh range.

3.4.2 Detection Setup

The detection axis consists of a similar setup to the setup used for imaging to characterise the light sheet. A 10x objective is used along with a 125 mm tube lens. The detection setup is aligned along the z-axis perpendicular to the plane of illumination.

This system is used to image the fluorescence from the sample. A Hamamatsu Orca-flash4.0 V3 camera is used as the detector. A filter (bandpass filer,405 ± 8 nm) is placed between the detection objective and the tube lens. This filter only transmits the fluorescent wavelengths from the sample and not the illumination wavelengths.

This setup is also used to image the profile of the light sheet as seen from the xy-plane. By placing a cuvette with fluorescent dye in the focal plane, the profile of the sheet can be seen. This allows the intensity distribution of the light sheet to be analysed.

Table 3.4: Hamamatsu Orca Camera Specifications

Pixel Array	2048×2048
Pixel Size	$6.5 \times 6.5\ \mu m^2$
Effective Area	$13.312 \times 13.312\ mm^2$
Full Res Max Frame Rate (fps)	40

3.4.3 Calibration of the Imaging Systems

The imaging setups are aligned and positioned such that a 50 μm calibration grid is in focus.

An image of this grid is then taken and used in order to calibrate the size that each pixel represents. This is achieved by averaging the total number of pixels between the minimum points on each line of the grid.

Figure 3.7: Image of the 50 μm grid obtained from the imaging system.

The blurring of the lines towards the edges of the image are typical of spherical abberations at larger imaging angles. The results of the calibration for the imaging and detection systems are shown in the table below.

Table 3.5: Calibration of the Imaging System. Here the Imaging system is aligned parallel to the sheet, while the detection axis is perpendicular to the sheet.

	Imaging System	Detection System
Mean seperation (pixels)	72	68
Standard Deviation (pixels)	1.8	1.1
Calibration μm per pixel	0.69	0.74

3.5 Samples

The samples available for our applications are fluorescent beads and a fluorescent dye. The fluorescent beads are used to generate three dimensional images to characterise the system, while the fluorescent dye is used to analyse the light sheets intensity distributions.

3.5.1 Fluorescent particles

Figure 3.8 shows that the light yellow particles have excitation wavelengths at around 400 nm and emission wavelengths at 450nm. This makes it a suitable sample for our system with an illumination wavelength of 405nm.

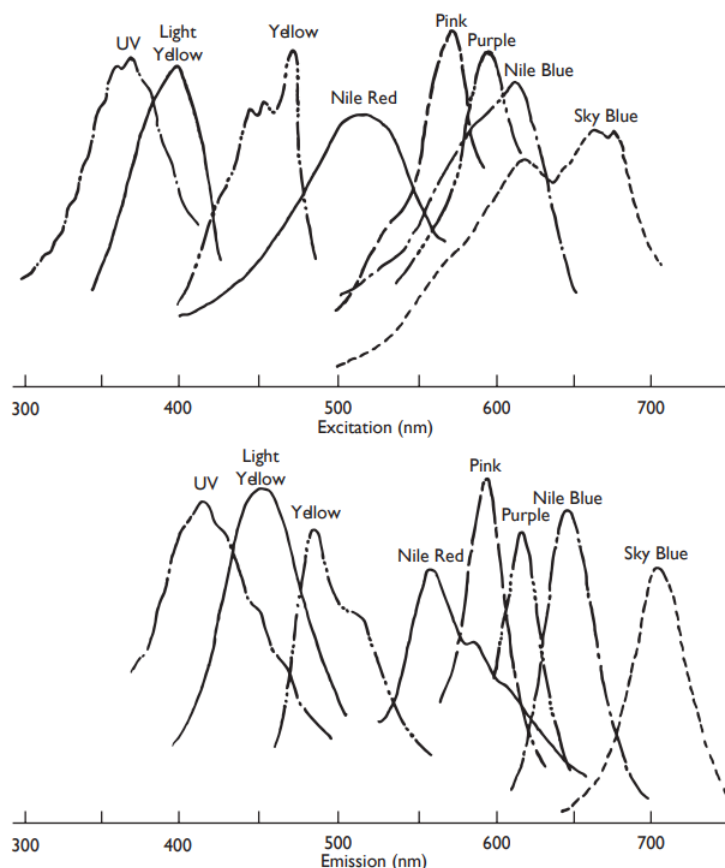The bead solution has a concentration of 1.0% w/v with nominal sizes ranging from 1.7-2.2 μm.

Figure 3.8: Excitation and emission for Spherotech fluorescent particles. Taken from: `https://www.spherotech.com/up_to_5.htm`. The "light yellow" particles are used in this study.

The samples are suspended in an agarose gel. The the agarose gel is prepared by heating 0.5-1% agarose disolved in distilled water. The particle solution is then mixed with the agarose solution in a 1:100 ratio. Capillaries with plungers are then used to draw the solution into the capillaries. Once the gel polymerises, the plunger can be used to push the gel out of the capillary. Only a small amount of the sample is pushed out of the capillary and mounted in the sample plane.

3.5.2 Fluorescent Dye

In addition to the fluorescent beads, we will also be using Rhodamine 6G disolved in ethanol. Rhodamine is a popular dye, designed to have large quantum yields, and as such is a prototypical sample for fluorescence applications.
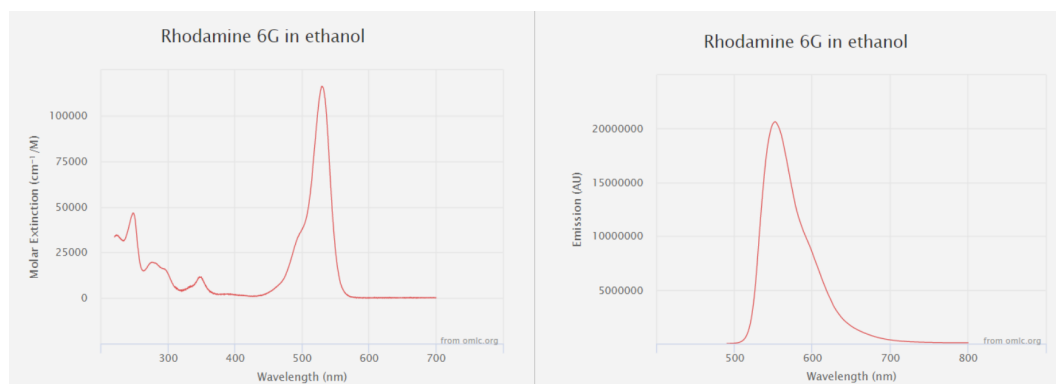
Figure 3.9: Excitation and emission spectrum for Rhodamine 6G in ethanol. Taken from url: `https://omlc.org/spectra/PhotochemCAD/html/083.html`

Chapter 4

Results And Discussion

The experimental results acquired for this study is presented in this chapter. The results for the characterisation of the various light sheet generation techniques are presented in sections 4.1 to 4.3. The implementation of the microscope to collect data of fluorescent bead sample, the three dimensional reconstruction of the data and the analysis of these images are discussed in section 4.4. Section 4.5 briefly discussed the results of deconvolution of the acquired data sets.

4.1 Characterisation of the light sheet generated with a cylindrical lens

The setup described in section 3.1 is first modelled in the simulation software General Laser Analysis and Design (GLAD) [29] before being implemented. The GLAD software allows the experimental setup to be simulated, where the propagation of the system can be analysed at various positions along the optical axis. The purpose of the simulation is to have some initial data which can be compared to the experimental results acquired in this setup.

The initial beam diameter incident at the aperture is 5 mm. A rectangular aperture is placed before the cylindrical lens with an aperture size of 5 mm.

The numerical aperture of the cylindrical lens with the rectangular aperture is given by

$$NA_{LS} = \frac{d}{f\sqrt{4 + \frac{d^2}{f^2}}} \tag{4.1}$$

where f is the focal length of the cylindrical lens and d is the diameter of the rectangular aperture.

The sheet radius is acquired at different positions (along the x-axis) from the focal point of the lens. The waist, ω_0 is then taken to be the smallest sheet radius. The field of view is then measured as twice the distance from the sheet waist to where the beam radius becomes $\sqrt{2}\omega_0$ as illustrated in figure 4.1
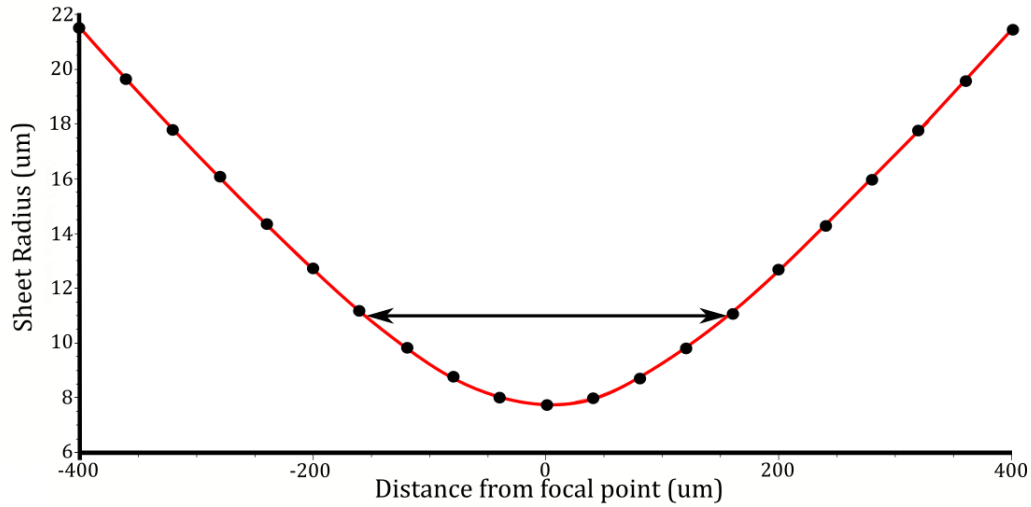

Figure 4.1: The simulated sheet radius at various positions from the focal point. The distance over which the sheet is approximately planar is illustrated by the arrow, where the beam radius increases to $\sqrt{2}\omega_0$.

With the simulation of the setup complete, we then implement the setup experimentally. With the imaging system, described in sections 3.4.1, positioned along the x-axis, images of the light sheet (in the yz-plane) are acquired at various positions away for the focal plane of the light sheet.
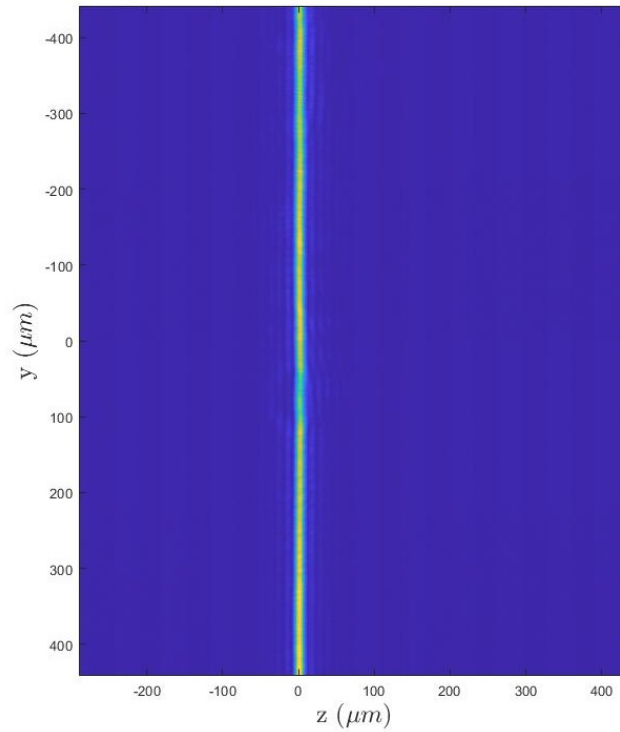
Figure 4.2: Cross section of the light sheet acquired at the focal plane of the sheet. The detector is aligned along the x-axis with the image in the yz-plane.

The images are analysed individually using MATLAB. Each image is integrated along the y-axis to acquire and average cross sectional profile (along the z-axis) of the sheet.

In order to approximate the central lobe, a Gaussian intensity profile, defined by

$$I(z) = I_o \exp(\frac{-2z^2}{w^2}), \tag{4.2}$$

is fitted to the data, from which the radius (w) of the beam is obtained.
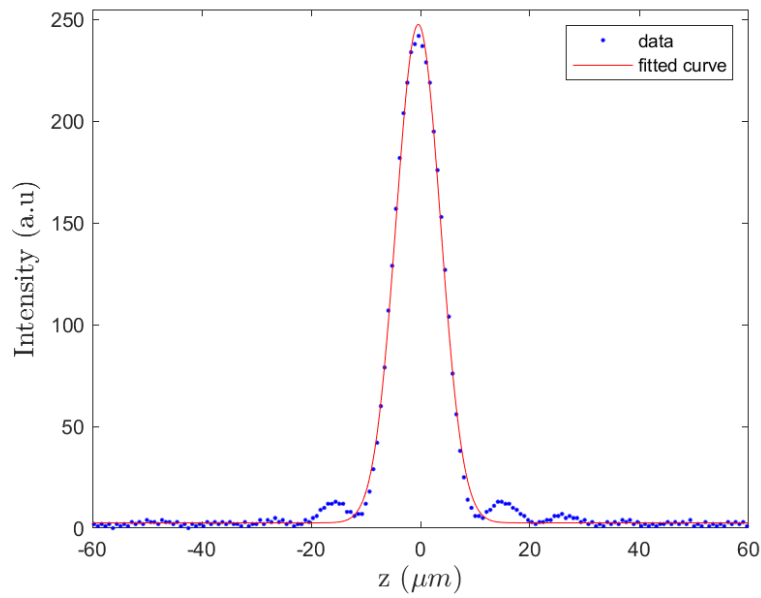
Figure 4.3: The cross sectional intensity profile of the light sheet at the focal plane is shown with the fitted curve from which the beam radius is obtained.

Repeating this process for each image, the radius of the sheet at various positions along the x-axis is acquired. Setting the smallest measured sheet radius as ω_0, the field of view can be measured, as before, by twice the distance from the focal plane to where the beam radius becomes $\sqrt{2}\omega_0$.
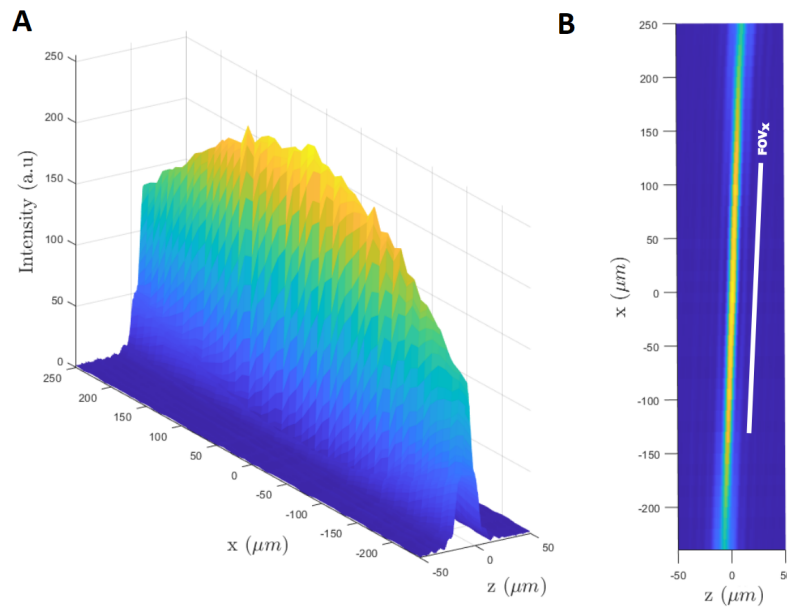
Figure 4.4: (A)Image of the light sheet scanned through the FOV. This image is generated using MATLAB by integrating each image along the y-axis in order to obtain the intensity profile along the z-axis at various positions of x. (B) A graph of the same data is taken in the xz-plane. The FOV along the x axis around the waist of the sheet is indicated.

Figure 4.4 clearly shows the maximum intensity near the focal point, as well as a visual indication of the sheets thickness and field of view.

The results of the simulated and theoretical light sheets are shown in the tables 4.1 and 4.2 below. The analytical expressions for the sheet waists and fields of view are described by equations 2.5 and 2.11 respectively.

Table 4.1: Experimental and simulated radius of the light sheet for various slit widths. Analytical calculations are included for comparison.

Slit Width (mm)	5	2	1	0.5
Experimental Radius (μm)	8.1	15.1	28.2	60.9
Simulated Radius (μm)	7.7	19.3	38.2	65.8
Analytical Radius (μm)	4.9	12.4	24.7	49.4

The data appears to agree with the theory,showing that an increase in slit width increases the numerical aperture, and therefore allows for smaller beam waists to be achieved.

The results in table 4.1, show that the simulation can be used to predict the sheet radius for various numerical apertures, while the analytical expressions appear to be less successful in predicting these waists.

The fields of view obtained for the various slit widths are shown in table 4.2. The analytical field of view described by equation 2.11 also shown. The values in brackets show the corresponding field of view obtained theoretically using the expression for the Rayleigh range,

$$FOV = 2X_R = \frac{\pi \omega_0^2 n}{\lambda} \tag{4.3}$$

for Gaussian beam propagation, where the waists measured in table 4.1 are used for ω_0.

Table 4.2: Experimental and simulated fields of view of the light sheets for varying slit widths. Analytical measurements are included for comparison. The values in brackets show the fields of views when Gaussian beam propogation is assumed.

Slit Width(mm)	5	2	1	0.5
Experiment (μm)	380 (1018)	1280 (3537)	3600 (12337)	17260(57539)
Simulated (μm)	350(920)	1950 (5779)	7650 (22639)	22350 (67170)
Analytical (μm)	289(380)	1803 (2368)	7210 (9470)	28837 (37876)

In table 4.2 we see that the field of view increases with a decrease in slit width. This is expected as the increase in slit width decreases the beam waist and therefore results in a decrease in the field of view. It is also worth noting that the results obtained in this table show large differences from the fields of view we would expect using Gaussian beam propagation. This is expected as the experimental beam experiences severe diffraction due to the overfilling of the back aperture.

A comparison between the experimental and simulated results, and the analytical calculations agree within an order of magnitude. As stated previously, this demonstrates the expected trend with varying NA. The quantitative predictive power of both the simulated and analytical results for our setup is limited for reasons eluded to at the end of this section.

Further comparison and verifications of the NA dependence follows. From equations 2.5 we have that the beam waist is given as

$$\omega_0 = \frac{0.61\lambda}{NA}. \tag{4.4}$$

If we fit the radius of the beams as a function of $\frac{1}{NA}$, we expect a linear function of the form $y = mx$, where the gradient is related to the equation above as

$$m = \alpha 0.61\lambda, \qquad (4.5)$$

where m is the gradient of the linear function and α is a constant.

Similarly for the FOV defined by equation 2.11, we can fit the measured fields of view as a function of $\frac{1}{NA^2}$, and define the gradient of the linear fit as

$$m = \beta 1.78\lambda. \qquad (4.6)$$

The results are shown in figures 4.5 and 4.6, with the resulting factors given in table 4.3
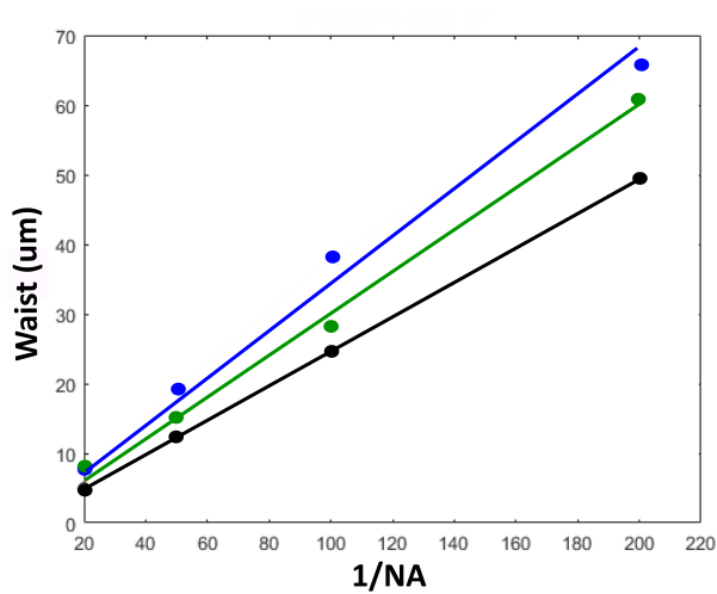

Figure 4.5: Fitting the beam waists as function of $\frac{1}{NA}$. The gradients of these functions are related to the analytical expression. Green is the experimental results, blue is the simulated results, and black is the analytical expression.

Figure 4.6: Fitting the fields of view as function of $\frac{1}{NA^2}$. The gradients of these functions are related to the analytical expression. Green is the experimental results, blue is the simulated results, and black is the analytical expression
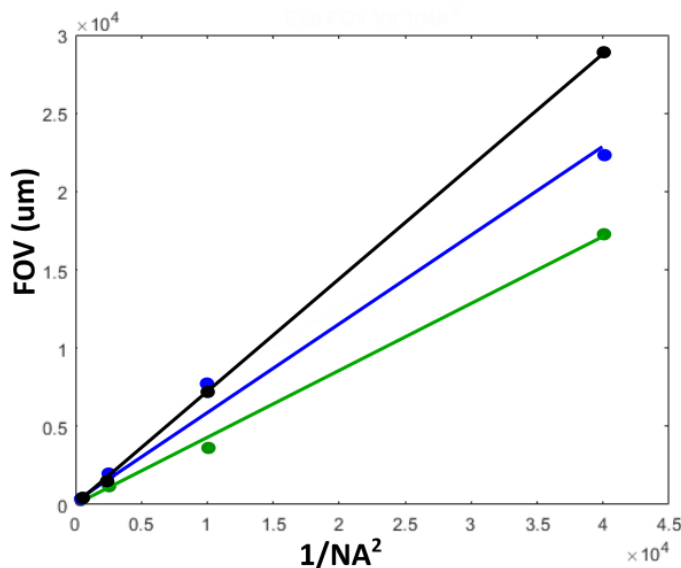
Table 4.3: The results for the fit for the radius and FOV of the sheet as a function of $\frac{1}{NA}$ and $\frac{1}{NA^2}$ respectively. The values in brackets are the R^2 values obtained from the fit

	Experimental	Simulation	Analytical
α	1.22 (0.989)	1.38 (0.979)	1
β	0.59 (0.996)	0.79 (0.985)	1

For both the experimental and simulated data, the results appear to follow the same relationships as defined by equations 2.5 and 2.11, as can be seen by the linear relationship when plotting the data as a function of $\frac{1}{NA}$ and $\frac{1}{NA^2}$.

The expected trends were present for both the fields of view and beam waists, which showed that a decrease in slit width (and therefore NA) produced wider beam waists and therefore wider fields of view.

We found that the experimental results qualitatively agrees well with both the simulated and analytical predictions, however we do notice discrepancies quantitatively. This is likely due to the fact that the analytical expression is diffraction limited, and this would therefore be the ideal case. Experimentally, there are many factors which contribute to these deviations, the primary influence not accounted for in the analytical diffraction theory or adequately

modelled in the simulations is spherical aberations, as experimentally we tend to overfill the back aperture of the illuminating objective . The GLAD software attempts to simulate these effects, however it is expected that the experimental measurements would be more prone to such factors.

As demonstrated by these results, manipulation of the light sheet is still possible using fixed optics by incorporating the variable aperture. However as seen in table 4.3, the experimental waists were found to be roughly 1.2 times larger than the expression 2.5 predicted, while the FOV's tended to be roughly 0.6 times the value predicted by equation 2.11. The equations in section 2.2 should therefore only be used as an approximation for the light sheet dimensions when choosing optics, after which the physical dimensions of the sheet should be measured experimentally.

4.2 SLM Generated Light Sheet

Using a cylindrical lens mask and grating, we are now able to generate a static light sheet at the focal plane of the illumination objective. The mask can then dynamically be adjusted using a grating mask to align the modulated light, while an aperture is used to block the unwanted light as explained in figure 2.6.

The central width of the cylindrical lens is adjusted such that the narrowest image is formed at the focal plane of the illumination plane. Adjusting the cylindrical lens central width shifts the focal plane after the fourier lens. In order to form the sheet correctly at the focal plane of the illumination objective, this central width needs to be selected such that the fourier image is formed near the focal plane of the fourier lens. This occured with a central width of 150 pixels. The setup used to analyse the resulting sheet is discussed in section 3.4.1 and is aligned along the x-axis.

Figure 4.7: Image of the light sheet at the focal plane generated by the SLM.

As in the previous section, a cross section of the averaged intensity distribution is plotted and the Gaussian expression given by equation 4.4 is fitted in order to measure the radius of the beam at various positions along x as shown in figure 4.8.
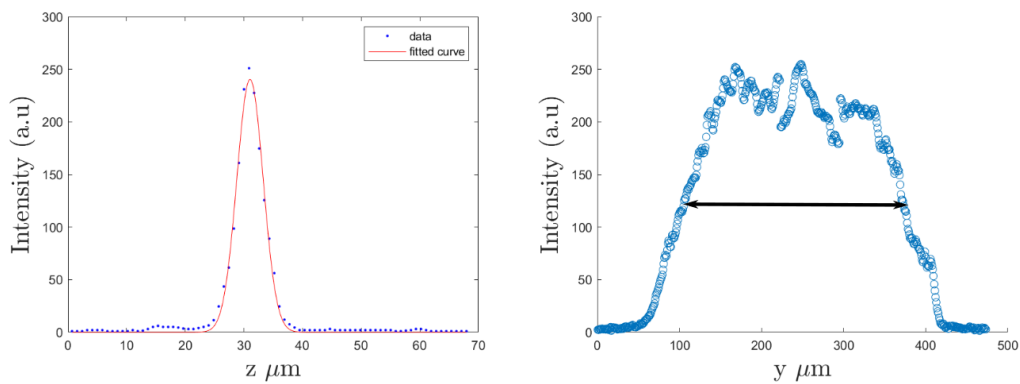

Figure 4.8: The averaged intensity profile of the sheet along the z and y axis. The sheet diameter can be extracted from image A, while image B indicates the distribution of the sheet at the focal plane from which the FOV in the y-axis can be measured as the FWHM of this distribution.

As illustrated in 4.8, the beams intensity distribution along the y-axis through the center of the sheet shows a relatively uniform distribution in the y-axis. The field of view along the y-axis is measured by the FWHM of the distribution. The results for the optimal light sheet for our setup is shown in table 4.4.

Table 4.4: The experimental results obtained using an SLM to generate a light sheet

Sheet Thickness (μm)	4.5
Field of View (μm)	150
Vertical Field of View (μm)	250
Power at Sample Plane (μW)	32

The beam diameter of 9 μm is an improvement over the sheet generated using a cylindrical lens. However the use of an aperture to select the desired parts of the fourier spectrum results in a short field of view along the y-axis and along the x-axis.

The peak power at the sample is measured to be approximately 32 μW, which is distributed throughout the sheet profile. The losses in power are primarily as a result of the phase modulation at the SLM, the presence of the beam splitter to separate the incident beam to and from the SLM, and the use of the aperture to select parts of the fourier spectrum for the light sheet.

4.3 Dynamically Scanned Light Sheets

Using the setup shown in figure 3.5 along with the same imaging system to characterise the sheet as in the previous two sections, the sheet thickness is measured and field of view is calculated in the same way as in the previous sections.

The parameters for the axicon mask are chosen to produce the narrowest possible sheet within the focal plane of the illumination objective. The central width for the generation of the Bessel beam is $d = 150$ pixels. In addition, an unmodulated Gaussian beam was scanned for comparison.
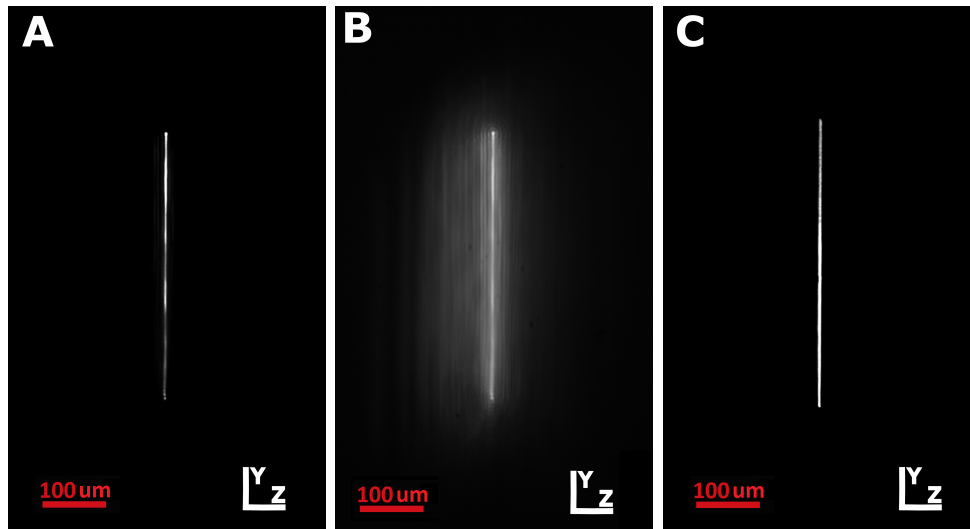
Figure 4.9: Scanned Bessel and Gaussian lightsheets imaged at the focal plane. A shows the Bessel beam light sheet. In B, the exposure time was increased to show the beam shape, which is visable at the turning points. The scanned Gaussian beam is shown in C

The Bessel and Gaussian beam profiles at the focal plane are shown in figure 4.9. By increasing the exposure time of figure A, the profile of the Bessel beam at the turning points can be seen as illustrated by figure B. The field of view along the y-axis can be changed independently of the other sheet dimensions based on the maximum voltage supplied to the galvo systems, however care should be taken when selecting the maximum amplitudes of the galvonometer, as at larger amplitudes, the angles from the propagation axis at the turning points are no longer parallel to the propagation axis.
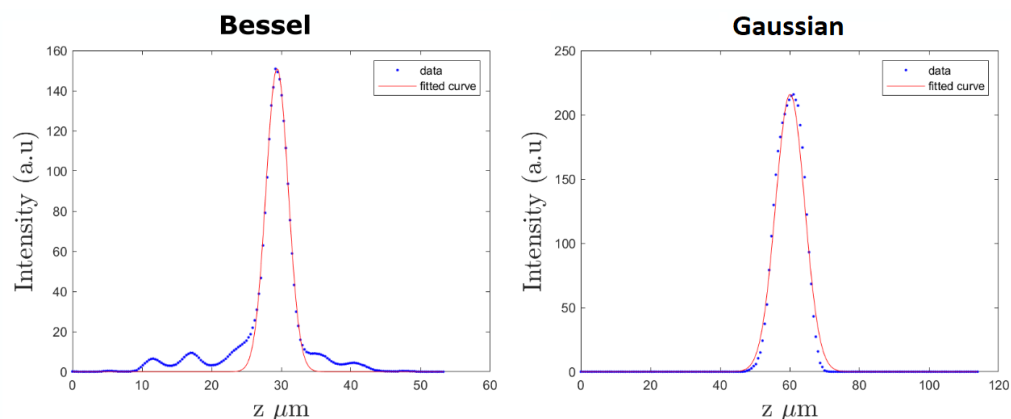

Figure 4.10: The averaged intensity profile of the sheets along the z-axis, from which the sheet diameter is measured.

Table 4.5: Experimental results for scanned sheet field of view and thickness

Beam Shape	Bessel	Gaussian
Sheet Waist μm	4.83	8.76
Field of View X μm	340	320

The average profile of the two scanned sheets at the focal plane are shown in figure 4.10. From the profiles, it can be seen that the beam radius of the Gaussian beam is almost doubled that of the Bessel beam.

The optimal beam diameters achieved using the Gaussian and Bessel beams are 17.52 μm and 9.66 μm respectively, but with fields of view 320 μm and 340 μm in the x-direction. As predicted by the theory on Bessel beams, we are able to obtain narrower light sheets with longer fields of view when using Bessel beams rather than Gaussian beams.

4.4 Sheet Intensity Distributions

Using a fluorescent dye (section 3.5.2) in a cuvette and placing it in the focus of the sheet, an image of the sheet along the detection axis is acquired. The camera's exposure time is set 100ms.
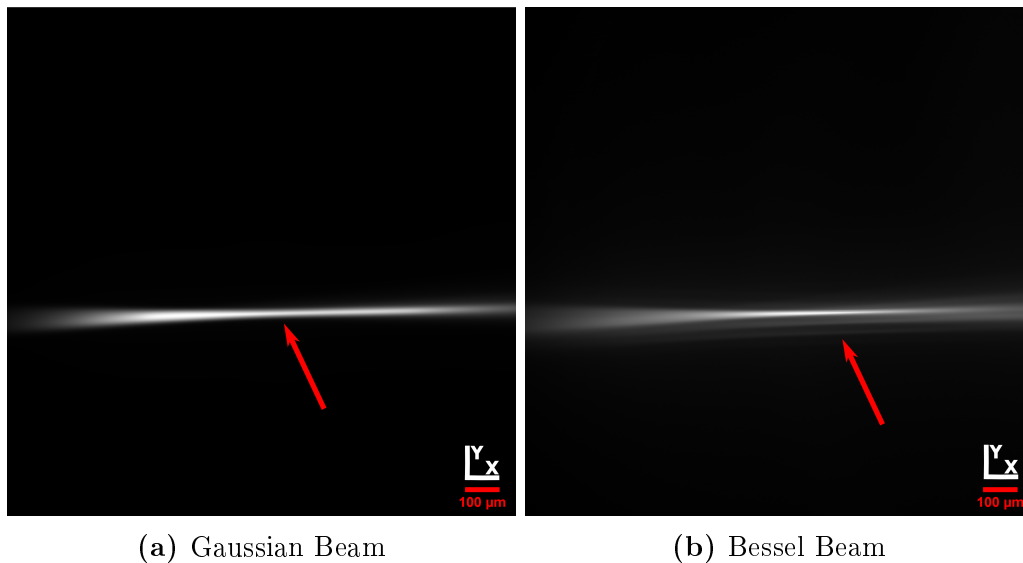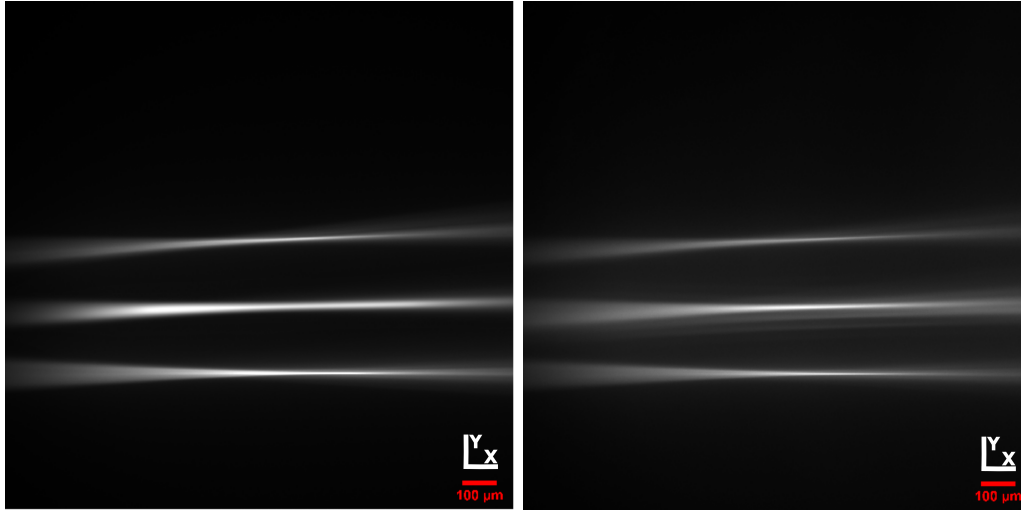

(a) Gaussian Beam   (b) Bessel Beam

Figure 4.11: Fluorescence image of the Gaussian and Bessel beam through the cuvette with fluorescent dye.

From figure 4.11 we can visualise the sheet thickness and field of view. Using these images, we an identify the positions of the focal points, however since

this is a fluorescence image, the sheet waists and field of view measured in the previous section will be used.

Using the previously measured fields of views we can select regions of interest around the focal points from which to analyse the distribution of the sheet.

These beams are then rapidly scanned by applying an amplitude of 1 mV at 1000 Hz ramp signal to the galvonometer mirrors. As explained in equation 2.36, the camera exposure time should be chosen in integer multiples of the scan period of the galvonometer.

(a) Gauussian Beam   (b) Bessel Beam

Figure 4.12: The Gaussian and Bessel beam propogation, imaged with the fluorescent dye in a cuvette. The images are generated by sending a constant amplitude signal to the galvonometers of -1 mV, 0 mV and 1 mV. The images are then superimposed to visualise the beam trajectory at different positions. The range -1 to 1 mV will then be used as the scanning range of the beam.

The amplitude of the signal sent to the galvonometer is chosen such that the beam remains parallel to the direction of propagation as shown in figure 4.12.
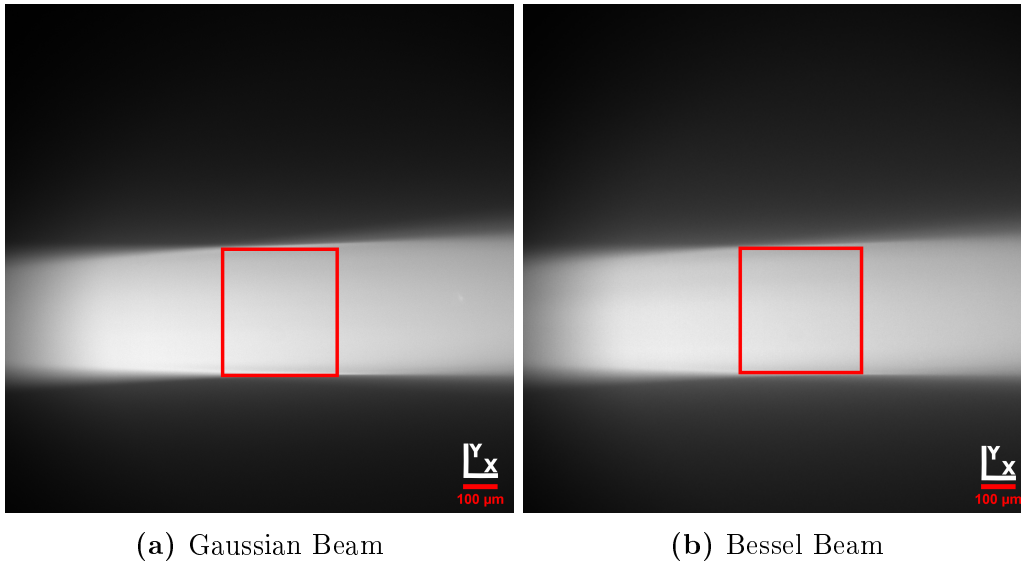
(a) Gaussian Beam   (b) Bessel Beam

Figure 4.13: The profile of the Gaussian and Bessel beam light sheets imaged using a fluorescent dye. The amplitude of the oscillations are 1 mV with frequency 1000 Hz. The regions of interest indicate the areas which will be selected when imaging samples.

By analysing the region of interests indicated in figure 4.13, the average intensity distribution of the sheet is acquired.
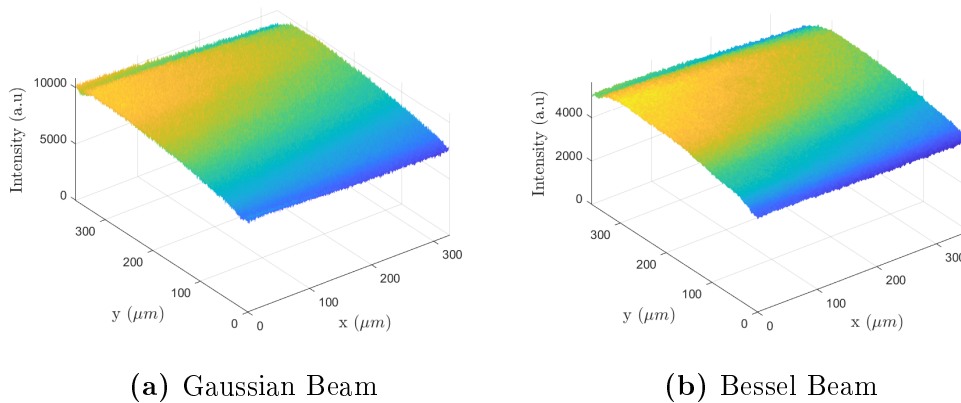

(a) Gaussian Beam   (b) Bessel Beam

Figure 4.14: The intenisty profile of the Gaussian and Bessel beam in the selected regions of interest around the focal plane.

From figure 4.14,we can visually see the uniformity of the light sheet in the regions of interest. Using the data in the figure can calculate the statistics of the sheet distributions as shown in table 4.6.

Table 4.6: Experimental measurements for the scanned sheet distribution

Stats	Bessel	Gaussian
Peak Power at the sample μW	78	121
Maximum Intensity Count	5626	10809
Minimum Intensity Count	4061	7141
Mean	5023	9248
Standard Deviation	311	666

From the data we find that under the same exposure time, the maximum intensity of the Gaussian beam is almost doubled the intensity of the Bessel beam sheet. This agrees with the measured power at the sample plane. The relative standard deviation for the Bessel and Gaussian scanned sheets are 5.53% and 6.16% respectively.
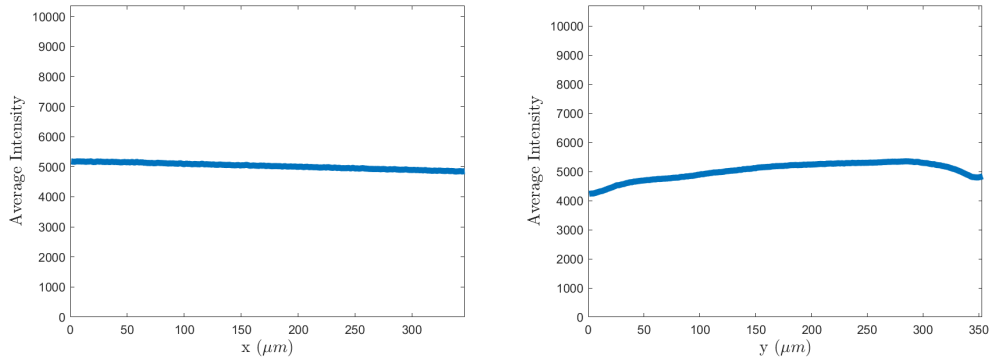
(a) Averaged cross section along x-axis **(b)** Averaged cross section along y-axis

Figure 4.15: Averaged cross section along x and y-axis of the Bessel sheet
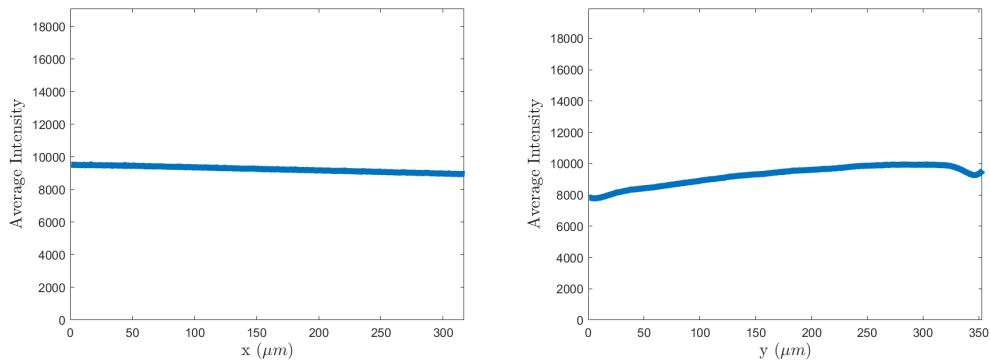
(a) Averaged cross section along x-axis **(b)** Averaged cross section along y-axis

Figure 4.16: Averaged cross section along x and y-axis of the Gaussian sheet

When displaying the average intensity distribution in the x and y-axis, as shown in figure 4.15 and 4.16, the profiles for both the Gaussian and Bessel beams along the x-axis has a linear decrease. This is due to the absorption of the fluorescent dye. In contrast we see that the distributions along the y-axis apears to drop off near the turning points of the scan. The regions of interest were chosen to avoid the edges of the light sheet, as such this likely induced as a result of the scanning angles introduced by the galvonometer. While the deviations of 5.53% and 6.16% maybe be considered large, we will assume this sheet to be uniform.

4.5 Limitations of Light Sheet Microscopy

One of the limitations of light sheet microscopy is shadow effects. When non-transparent objects pass through the sheet, they cause shadows behind the object. This reduces the imaging capabilities behind the object. Figure 4.17 shows and image of this phenomenon captured while analysing the sheet through the fluorescent dye.
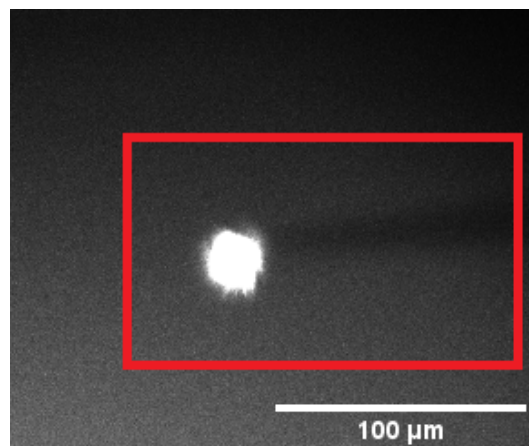

Figure 4.17: Shadow effects caused by nontransparent particles in the fluorescent dye used to analyse the sheet profiles.

To analyse the effect of the shadow, a line out, along the y-axis, 30 μm to the left of the center of the particle and 30 μm to the right of the particle is taken. Intensities to the left and right of the particle (along the y-axis) are recorded. The ratio of intensities between the two sets of data are then plotted as shown in figure 4.18.
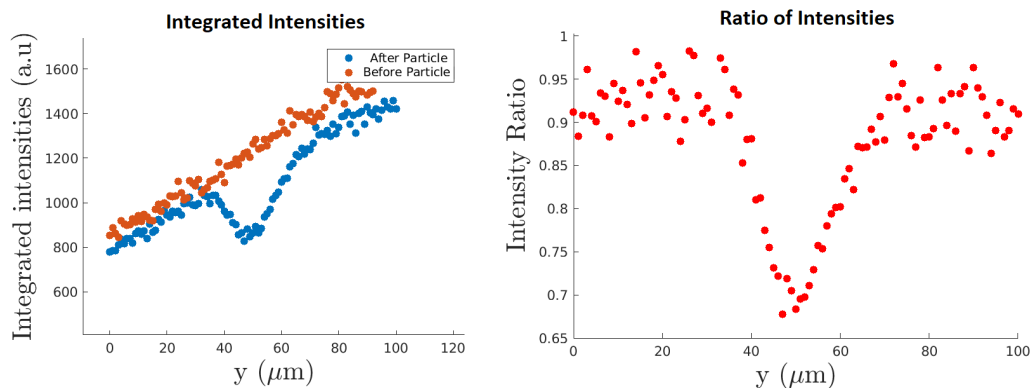
Figure 4.18: The integrated intensities before and after the non-transparent particle are shown. The ratio of the intensities before and after the particle are calculated and plotted to show a drastic decrease in the intensities in the regions directly behind the non-transparent object.

When analysing the results in figure 4.18 we find that in the region behind the particle, the intensity drops to approximately 70% of the intensity in the regions which are unobstructed by the particles.

Shadow effects therefore reduced the ability of the microscope to image structures behind non-transparent objects. One way to avoid this is by the use two-sided illumination [30].

4.6 Imaging Fluorescent Particles

A 1% agarose solution is prepared with 1% particle solution. The agarose gel is mounted from a capillary in the light sheet.
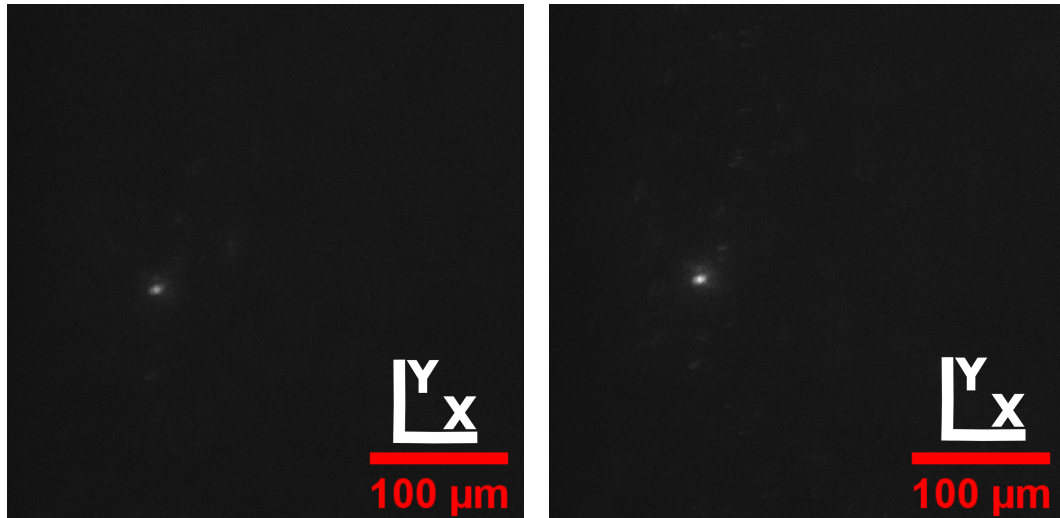
Figure 4.19: Fluorescence images taken using the Bessel (left) and Gaussian (right) beams for illumination.

The images acquired in figure 4.19 are taken at the same positions along the z-axis with the same exposure time of 100 ms. The fluorescence of the same particles can be seen, with more particles visible when illuminated with the Gaussian beam. This is due to the wider sheet thickness and higher intensity of the Gaussian sheet.
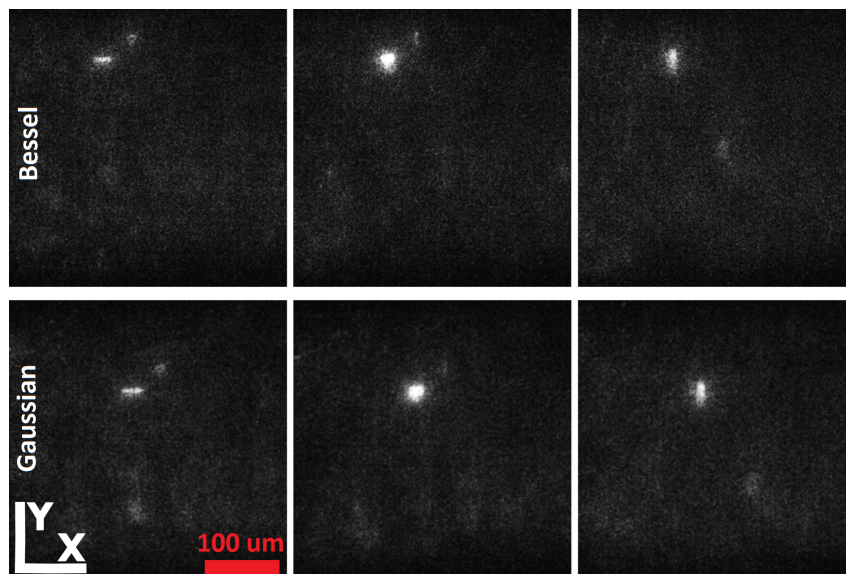

Figure 4.20: The behavior of the fluorescence of particles, illuminated with a Bessel (top) and Gaussian (bottom) lightsheet, when translating the sample at -35 μm, 0 μm and 35 μm along the z-axis.

Figure 4.20 shows the fluorescence of a cluster of particles changing shape from a horizontal ellipse before the cluster is in focus, to a vertical ellipse behind the cluster. This is a result of the astigmatism of the imaging setup. This is likely caused by the curvature of the agarose gel in which the particles are embedded. The agarose gel takes on the same shape as the cylindrical capillary in which it is prepared. The samples are subject to diffraction, as the agarose has a refractive index of 1.3.

4.6.1 Three-dimensional reconstruction

Acquiring multiple images by the sample to various positions along the z-axis allows us to reconstruct the fluorescence of the scanned regions. Images are acquired at 100 ms exposure times, with each slice along the z-axis taken 5 μm apart. The three-dimensional image is constructed using an ImageJ plugin called volume viewer. The data is interpolated using the nearest neighbours method. The nearest neighbour method selects the value from the nearest point, and does not consider the value of the points surrounding that nearest point. A transfer function can be applied for visualisation. Applying a threshold allows us to identify particles more clearly.
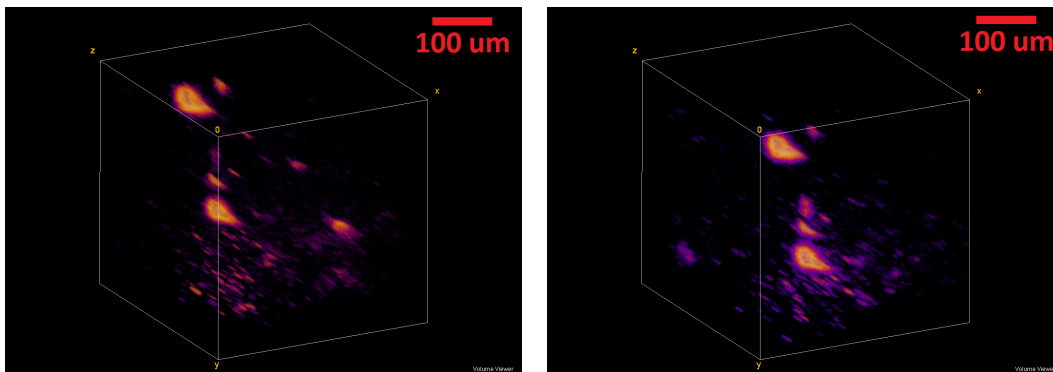

Figure 4.21: Three dimensional reconstruction of the fluorescent particles in the sample illuminated with a scanned Bessel (left) and Gaussian (right) light sheet.

The reconstructed images in figure 4.21 clearly show the positions of the particles in the sample. The scans for both beams were conducted across the same positions for both the Bessel and Gaussian sheets.

4.6.2 Analyses The 3D models

By reducing the threshold of the three dimensional images, light in the agarose can be shown. When viewed from the angle as shown in figure 4.22, the cylindrical shape of the agarose can be seen. This will influence the shape of the

fluorescence images, and would contribute to the artifacts of the particles transforming from a horizontal ellipse before the particle is focused, to a vertical ellipse after the particles as seen in figure 4.20.
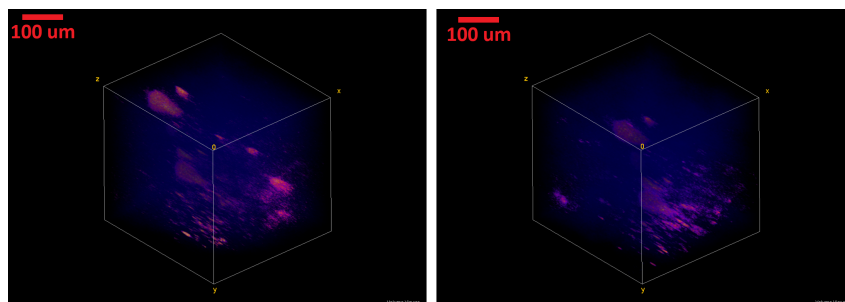

Figure 4.22: 3D image of the sample using the Bessel(left) and Gaussian(right) light sheets. The cylindrical curvature of the agarose is visible in the lower left corner.
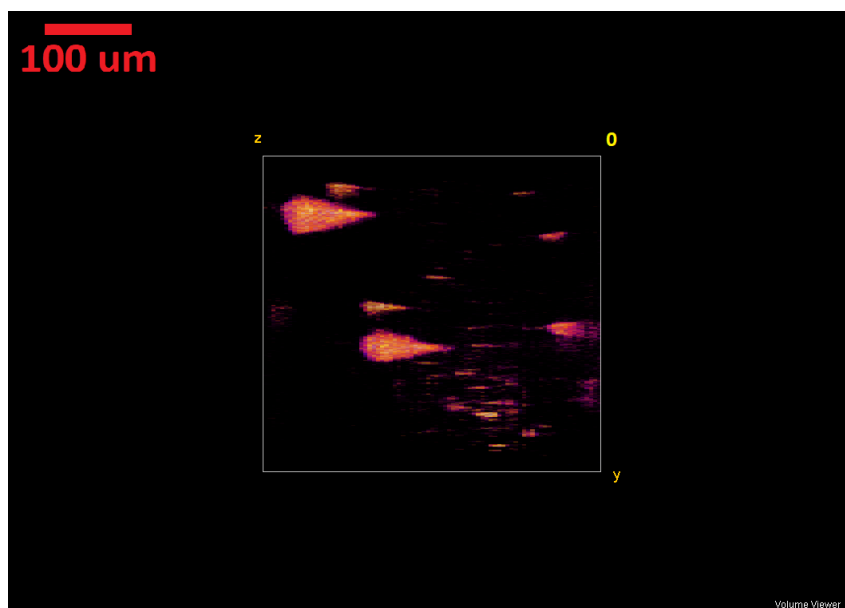

Figure 4.23: 3D image generated using the Bessel beam viewed along the yz-plane.

Figure 4.23 shows the image viewed along the yz-plane with the detection camera to the right of the image. There is an asymmetry in the image. To the left of the image, large clusters of particles are visable with streaks trailing to the right of the clusters, while on the right of the image, there are smaller clusters with streaks trailing to the left. The streaks trailing to the left of the image may be caused by the curvature effects of the agarose, which has a cylindrical shape. The clusters on the left of the image has trails to the right.

These are especially prominent on the largest clusters, and is assumed to be caused by re-absorption in these large clusters.

The clusters near the center of the image appear to have a more uniform, elongated shape. We can assume some of these small clusters to be individual particles or clusters containing very few particles. By manually identifying and isolating a few particles, we can analyse their shapes.
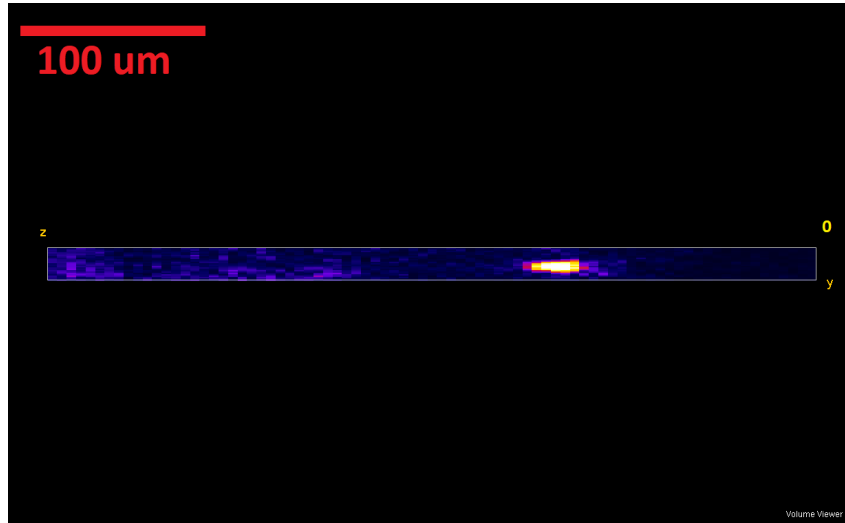

Figure 4.24: Sliced image of an isolated particle.

Figure 4.6.2 shows a slice along the yz-plane through a selected particle. By analysing the profile through the particle along the z-axis, the FWHM of the particle can be acquired. Individual particles have a smaller diameter than the light sheet, and this therefore means that the FWHM along the z-axis of these elongated particles are a representation of the sheet thickness. This is done for a variety of particles from the models generated using both the Bessel and Gaussian light sheets. The results are presented in figure 4.6.2.
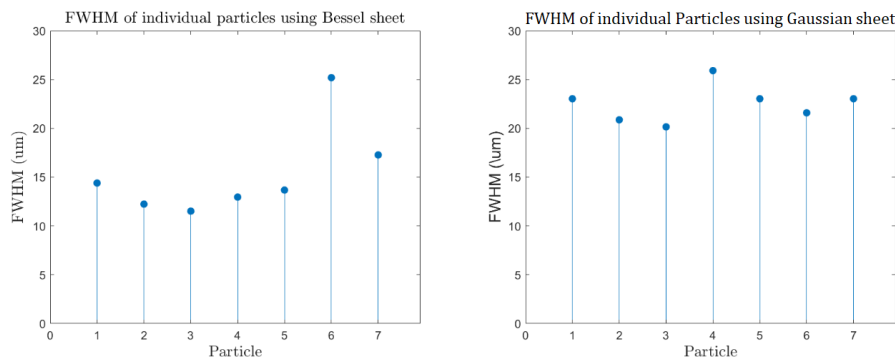
Figure 4.25: FWHM along the z-axis through the center of isolated particles or small clusters of particles identified in the three dimension images obtained using the Bessel (left) and Gaussian (right) sheet.

Table 4.7: Measured FWHM (μm) for individual particles in the 3D models.

Stats	Bessel	Gaussian
Mean FWHM (μm)	13.6	22.5
Standard Deviation (μm)	2	1.89

The waists of the sheets for the Bessel and Gaussian beams measured in section 4.4 where 4.83 μm and 8.76 μm respectively. These sheets where approximated as planar over the regions where their waists are less than $\sqrt{2}\omega_o$. The diameters of the sheets across their fields of view are therefore between 9.7 μm and 13.7 μm for the Bessel beam and 17.5 μm and 24.8 μm.

The results shown in table 4.7 show that the FWHM of the individual particles fall within the range of the sheet thickness. The length of the elongated particles are therefore a good indication of the sheet diameter.

4.7 Deconvolution

With the analysis of the raw data complete, we now implement the image restoration technique using the LSDeconv software.

The software takes in the parameters of the light sheet and the detection system. In our system our detection objective is a 10x objective with a numerical apperture of 0.2.

The results of the implementation on the data obtained with the scanned Gaussian and scanned Bessel beam are shown in figure 4.26

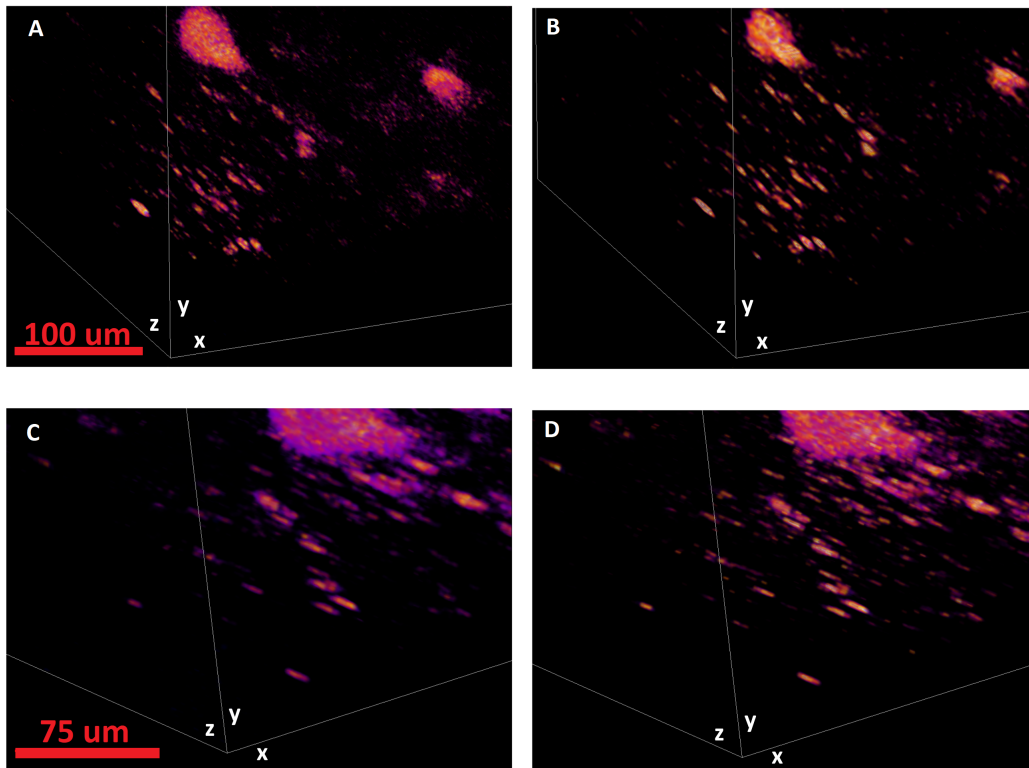**Figure 4.26:** Results obtained after deconvoling the raw data using LSDeconv software. A and B shows the original and deconvolved results obtained with the Bessel beam respectively. Figure C and D show the original and deconvolved results obtained with the Gaussian beam respectively.

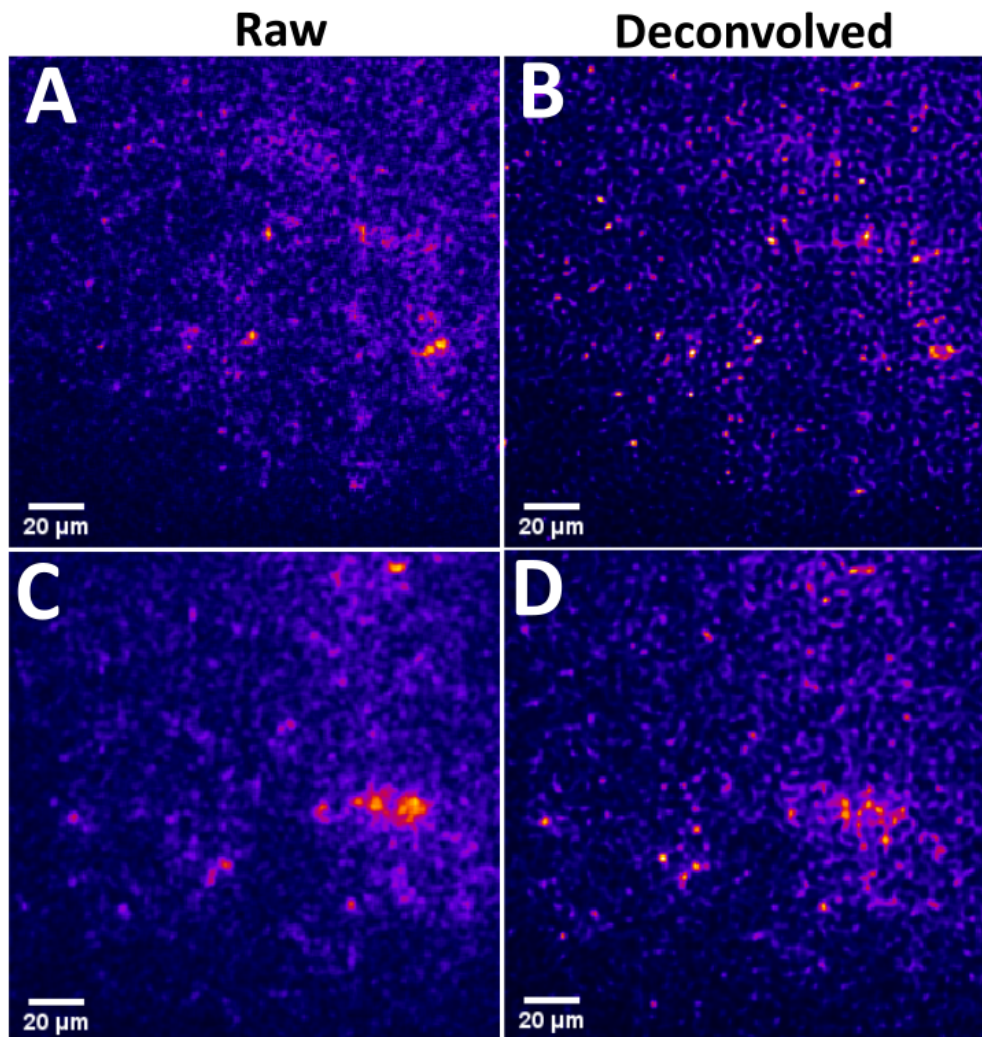By taking a slice along the xy-plane through the images, we can compare the effects of the deconvolution on the data.

Figure 4.27: Single Slices at the same xy-plane for the raw data and the deconvolved data. A and B show the raw and deconvolved images at the same plane for the image generated with the Bessel beam. C and D show the raw and deconvolved data for the image generated with the Gaussian beam.

From figure 4.27, there is a clear difference for both the images after applying the deconvolution. We see a noticeable increase in the sharpness of the image. When comparing the images of the deconvolution in A and B, we are able to identify more particles after the deconvolution. Similarly the small cluster present near the right of the image in C and D, shows the particles around this small cluster more clearly.

Taking a cross section through small particles in each set of data, we can observe that change in the particles image as a result of the deconvolution.
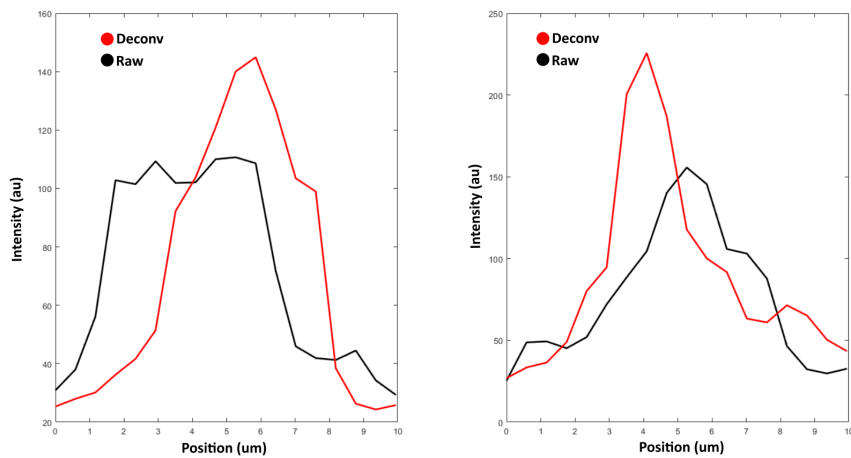
Figure 4.28: The cross sections for a single particle identified for the deconvolved and raw data. The figure on the left shows the Gaussian results, while the right figure shows the results using the Bessel beam.

If we take the FWHM of these data points, we find that the deconvolution improved the quality of the Gaussian beam image, with the FWHM of the same particle decreasing by approximately 1 μm, while the intensity increased. In the results for the Bessel beam, we find that the selected particles size decreased by approximately 2 μm, with a noticeable increase in intensity.

These results suggest that the process of deconvolution does indeed improve the quality of images generated with light sheet microscopy.

Chapter 5

Conclusions

The three illumination techniques used in light sheet microscopy have been studied. Theory on the parameters used to characterise the light sheet microscope capabilities were introduced. The characterisation of the techniques were done experimentally using commercially available optics.

The generation of light sheets using cylindrical lenses proved to be an effective method for use in microscopy, with beam diameters of up to 16 μm with FOV of 380 μm. While the setup allowed for the manipulation of the sheet using the slit to control the numerical aperture, and thereby control the sheet's thickness, the set optics available restricted the resolutions which could be achieved.

The introduction of the SLM introduced more freedom with which to tailor the light sheet, allowing for the generation of a light sheet with a beam diameter of 9 μm and field of view along the x-axis of 150 μm. The draw back of this implementation was the low power at sample of 32 μW distributed through out the sheet.

A suitable middle ground was found using digitally scanned light sheets. Light sheets using Gaussian and Bessel beams were implemented, which achieved beam diameters of 17.6 μm and 9.6 μm respectively, and peak power at the samples of 121 μW and 78 μW. The results showed that the use of Bessel beams allowed for narrower sheets with larger fields of view to be generated when compared to Gaussian beams. By using the SLM for beam shaping and scanning the beam rapidly, a sheet can be formed which has the freedom to be tailored, with the scanning allowing the full power at the sample to be available at each site during the scanning process. The intensity distributions showed that the beam profiles during a single expose time with scanned beams remained uniform across the field of view.

Light sheets using scanned Gaussian and Bessel beams were used to image samples, which allowed for shorter exposure times. Images were acquired at 100 ms exposure times, with the galvonometer systems scanning the beam at 1 kHz. The resulting images showed the capabilities of the system to capture

three dimensional fluorescence images. Light sheet microscopes are designed according to the dimensions of the desired sample. Direct comparison between the capabilities of different systems is therefore not possible. However, with the simple optics used, the system was still able to obtain a good resolution.

The LSDeconv software proved to be a useful tool for image reconstruction in light sheet microscopy, as noticeable improvements where could be seen visually. When observing the sizes of individual particles, the decrease in the particle size after the deconvolution suggests that the deconvolution process improves resolution by reassigning distorted light back to its source.

The setup in its current form can be improved. The incorporation of two-sided illumination can be used to reduce shadow effects [30] seen in section 4.5. Additionally, two-photon excitation, using longer wavelengths of light, can be used to reduce scattering and improve the signal to noise ratio, allowing for increased penetration depths within the sample [31].

Bibliography

[1] Sanderson, M., Smith, I., Parker, I. and Bootman, M.: Fluorescence microscopy. *Cold Spring Harbor Protocols*, 2014.

[2] Magidson, V. and Khodjakov, A.: Circumventing photodamage in live-cell microscopy. *Methods Cell Biol*, vol. 114, 2013.

[3] Rice, G.: Fluorescent microscopy. *Montana State University*, 2019.

[4] Kubitscheck, U.: *Fluorescence Microscopy: From Principles to Biological Applications: Second Edition.* 2017.

[5] Rost, F.: Fluorescence microscopy, applications. *Encyclopedia of Spectrocopy and Spectrometry*, 2010.

[6] Vicente, N., Diaz Zamboni, J., Adur, J., Paravani, E. and Casco, V.: Photobleaching correction in fluorescence microscopy images. *Journal of Physics: Conference Series*, vol. 90, 2007.

[7] Ulrich, K., Kuckmann, O., Kues, T. and Peters, R.: Imaging and tracking of single gfp molecules in solution. *Biophysical Journal*, vol. 78, 2000.

[8] Borlinghasu, R. and Hass, P.: Confocal and digital light sheet imaging. *Leica Microsystems*, 2015.

[9] Keller, P. and Stelzer, E.: Digital scanned laser light sheet fluorescence microscopy(dslm). *Cold Spring Harbor Protocols*, vol. 2010, 2010.

[10] Santi, P.: Light sheet fluorescence microscopy: A review. *Journal of Histochemistry and Cytochemisty*, vol. 59, 2011.

[11] Garwin, L. and Linc: The first laser. *A Century of Nature: Twenty-One Discoveries that Changed Science and the World*, 2008.

[12] Voie, A., Burns, D. and Spelman, F.: Orthogonal-plane fluorescence optical sectioning: Three-dimensional imaging of macroscopic biological specimens. *Journal of Microscopy*, vol. 170, 1993.

[13] Tomer, R., Lovett-Barron, M., Kauvar, I., Andalman, A., Burn, V., Sankaran, S., Grosenick, L., Broxton, M., Yang, S. and Deisseroth, K.: Sped light sheet microscopy: Fast mapping of biological system structure and function. *Cell*, vol. 163, 2015.

67

[14] Olarte, O., Andilla, J., Gualda, E. and Loza-Alvarex, P.: Light-sheet microscopy: a tutorial. *Advances in Optics and Photonics*, vol. 10, 2018.

[15] Reynaud, E., Krzic, U., Greger, K. and Stelzer, E.: Light sheet-based fluorescence microscopy: more dimension, more photons, and less photodamage. *HFSP Journal*, vol. 2, 2008.

[16] Gao, L., Shao, L., Chen, B. and Betzig, E.: 3d live fluorescence imaging of cellular dynamics using bessel beam plane illumination microscopy. *Nature Protocols*, vol. 9, 2014.

[17] Hecht, E.: *Optics: Global Edition*. 2017.

[18] Latychevskaia, T.: Lateral and axial resolution criteria in incoherent and coherent optics and holography, near- and far-field regimes. *Applied Optics*, vol. 58, 2019.

[19] Goodman, J.: *Introduction to Fourier Optics*. 1996.

[20] Samuylov, D., Purwar, P., Szekely, G. and Paul, G.: Modelling point spread function in fluorescence microscopy with a sparse gaussian mixture: trade-off between accuracy and efficiency. 2019.

[21] Jullien, A.: Spatial light modulators. *Photoniques*, 2020.

[22] Zhai, Z., Cheng, Z., Lv, Q. and Wang, X.: Tunable axicons generated by spatial light modulator with high-level phase computer-generated holograms. *Applied Sciences*, vol. 10, 2020.

[23] Sibarita, J.: Deconvolution microscopy. *Advances in biochemical engineering/biotechnology*, vol. 95, 2005.

[24] Becke, K., Saghafi, S., Pende, M., Sabdyusheva, I., Hahn, C., Foroughipour, M., Jahrling, N. and Dodt, H.: Deconvolution of light sheet microscopy recordings. *Scientific Reports*, vol. 9, 2019.

[25] Laasmaa, M., Vendelin, M. and Peterson, P.: Applications of regularised richardson-lucy algorithm for deconvolution of confocal microscopy images. *Journal of microscopy*, 2011.

[26] Aakhte, M., Akhlaghi, E. and Muller, H.: Sspim: a beam shaping toolbox for structured selective plane illumination microscopy. *Scientific Reports*, vol. 8, 2018.

[27] Li, R. and Cao, L.: Progress in phase calibration for liquid crystal spatial light modulators. *Applied Sciences*, vol. 9, 2019.

[28] Spangenberg, D., Dudley, A., Neethling, P., Rohwer, E. and Forbes, A.: White light wavefront control with a spatial light modulator. *Optics Express*, vol. 22, 2014.

[29] General laser analysis and design (glad). `http://www.aor.com/`. Accessed: 2020.

[30] Santi, P.: Light sheet fluorescence microscopy a review. *Journal of Histochemistry and Cytochemistry*, vol. 59, 2011.

[31] Piksarv, P., Marti, D., Le, T., Unterhuber, A. and Forbes, L.: Integrated single- and two-photon light sheet microscopy using accelerating beams. *Scientific Reports*, vol. 7, 2017.